Structural analysis of a motor with increased mechanical output reveals new transitions in kinesin microtubule motility

Shibata, Satoki ; Wang, Matthew Y. ; Imasaki, Tsuyoshi ; Shigematsu, Hideki ; Ugarte La Torre, Diego ; Wei, Yuanyuan ; Jobichen, Chacko ;…

(Citation)
Scientific Reports,16(1):487

(Issue Date)
2026-01-05

(Resource Type)
journal article

(Version)
Version of Record

scientific reports

Check for updates

OPEN

Structural analysis of a motor with increased mechanical output reveals new transitions in kinesin microtubule motility

Satoki Shibata[1,9], Matthew Y. Wang[2,9], Tsuyoshi Imasaki[1,9]✉, Hideki Shigematsu[3], Diego Ugarte La Torre[4], Yuanyuan Wei[5], Chacko Jobichen[6,8], Hajime Hagio[1], J. Sivaraman[6], Yuji Sugita[4,7], Sharyn A. Endow[2,5]✉ & Ryo Nitta[1]✉

Kinesin motors use ATP to produce force in cells, yet the conformational changes that generate force remain uncertain. Here, we report structural and mechanistic insights into a minus-end-directed kinesin-14 that exhibits increased mechanical output – the variant motor binds microtubules more tightly and moves with faster velocity than wild type. High-resolution structures, together with molecular dynamics simulations, reveal previously unobserved transitions in the nucleotide hydrolysis cycle. ADP release, triggered by microtubule binding, is coupled to twisting of the central β-sheet and stabilization of the stalk prior to the power stroke. ATP binding induces stalk fluctuations and a swing of the neck mimic, an element analogous to the kinesin-1 neck linker, resembling neck linker docking in plus-end-directed kinesins. The power stroke, characterized by a large stalk rotation, is followed by motor detachment from microtubules. The subsequent recovery stroke occurs while the motor is bound to ADP and free Pi, accompanied by β-strand-to-loop transitions, or β-sheet melting, implying that β-sheet refolding facilitates Pi release. The observed twisting and melting identify the central β-sheet as the long-sought elastic element or spring required for motor force production. The transitions we observe in kinesin-14 may also apply to other kinesins – this remains to be tested.

Keywords Motor force production, Power stroke fluctuations, Neck mimic docking, ADP + free Pi state, Beta-sheet distortion, Motor spring-like element

Motor proteins – the dyneins, myosins, and kinesins – hydrolyze ATP and bind to microtubules or actin filaments, producing force and steps along their filament, or sliding of filaments relative to one another. The mechanism by which motor proteins produce force and movement is still not fully understood. The motor force-generating mechanism is known to rely on ATP binding, hydrolysis, and release of hydrolysis products, coupled to filament binding and release[1]. This has led to the idea that motility is regulated by the nucleotide state of the motor, together with motor-filament interactions[2,3]. Motors have been hypothesized to contain a spring-like or elastic element that compresses in a specific nucleotide state, storing free energy, and then releases in a subsequent state, producing force[1], but the spring has not yet been definitively identified. The movements in the motor domain due to nucleotide binding, hydrolysis, and product release are small, based on kinetic studies of myosin[4], a motor evolutionarily related to the kinesin family[5], and other ATP-binding enzymes[6]. This has also been observed in structural studies of myosin in different nucleotide states[3,7].

[1]Division of Structural Medicine and Anatomy, Department of Physiology and Cell Biology, Kobe University Graduate School of Medicine, 650-0017 Kobe, Japan. [2]Department of Cell Biology, Duke University Medical Center, Durham, NC 27710, USA. [3]Structural Biology Division, Synchrotron Radiation Research Institute, SPring- 8, Sayo, Hyogo 679-5184, Japan. [4]Computational Biophysics Research Team, RIKEN Center for Computational Science, 650-0047 Kobe, Japan. [5]Neuroscience & Behavioral Disorders Programme, Duke-NUS School of Medicine, 169857 Singapore, Singapore. [6]Department of Biological Sciences, National University of Singapore, 117558 Singapore, Singapore. [7]Theoretical Molecular Science Laboratory, RIKEN Pioneering Research Institute, Saitama 351-0198, Japan. [8]Present address: School of Chemistry and Molecular Bioscience, University of Queensland, Brisbane, QLD 4072, Australia. [9]Satoki Shibata, Matthew Y. Wang and Tsuyoshi Imasaki contributed equally to this work. ✉email: ima3@med.kobe-u.ac.jp; endow@duke.edu; ryonitta@med.kobe-u.ac.jp

The kinesins produce a power stroke, but the structural element that functions as a lever to amplify force produced by the motor differs for kinesin-1 and kinesin-14, motors that move in opposite directions on microtubules. Kinesin-1, the first-discovered kinesin, is a highly processive motor that moves towards microtubule plus ends[8–10]. The kinesin-1 power stroke is thought to consist of a large change in conformation of the neck linker, a short region (~ 13 amino acids) that joins the conserved motor domain to the α-helical coiled-coil stalk[11,12]. Upon ATP binding, the neck linker binds to, or docks, onto the motor domain, but is mobile after ATP hydrolysis and Pi release. A second short region (~ 11 amino acids) at the N terminus of the conserved motor domain, the cover strand, forms a β-strand (β0) that binds to the neck linker during force production[11,13].

By contrast, kinesin-14 Ncd is a motor of low processivity that binds to microtubules and produces displacements towards the microtubule minus end, differing from kinesin-1. The Ncd coiled-coil stalk in crystal structures of the dimeric motor shows a large ~ 75–80° rotation towards the microtubule minus end[14–17], resembling the swing of the myosin lever arm[18,19]. A large displacement by Ncd observed in laser-trap assays and the dependence of motor velocity on the length of the stalk support the hypothesis that the Ncd stalk functions like a lever[14,20,21]. The kinesin-14 stalk is thus thought to produce the working stroke of the motor. A short region (10–11 amino acids) at the kinesin-14 C terminus, the neck mimic, is also thought to contribute to the motor power stroke[22,23]. This region is analogous to the kinesin-1 neck linker[24]. However, unlike the kinesin-1 neck linker, the kinesin-14 Ncd neck mimic is largely disordered in previous crystal structures.

Although basic features of force production by the kinesins have been reported, key steps in the motor mechanism are still not known, including the residues involved in mechanochemical coupling and the conformational changes that occur upon microtubule binding and nucleotide release, triggering the power stroke. Studies on myosin identified the α-helical light-chain binding region immediately adjacent to the conserved motor domain as a lever-like element that produces a power stroke by undergoing a large rotation, amplifying small movements of structural elements in the conserved motor domain[19,25]. Nucleotide-free, rigor-like crystal structures reported for myosin and unconventional myosin V revealed distortional movements of the central β-sheet that rearrange the motor actin-binding region and reduce motor affinity for nucleotide prior to the power stroke[26,27]. We proposed previously that, like myosin, the central β-sheet of the kinesins undergoes structural changes involved in ADP release and force generation[28]. We identified a highly conserved residue of the kinesin motor domain in a loop of the central β-sheet that could couple microtubule binding and release to ATP hydrolysis[29]. Variants of kinesin-14 Ncd that affect this residue, Y485, bind more tightly to microtubules than wild-type – the motors show increased microtubule binding affinity and weaker ADP binding, which is coupled to microtubule binding in the kinesin motors. This results in faster ATP hydrolysis, which, in turn, causes faster movement in gliding assays[29] without changing the motor mechanochemical cycle. The largest effects were observed for the NcdY485K variant, which causes the assembly of longer than normal oocyte spindles in vivo, providing evidence for the gain-of-function effects of the motor in live cells.

We undertook structural studies on the kinesin-14 NcdY485K motor to determine the structural changes that cause the changes in motor binding to microtubules and nucleotide. We observe features that have not been reported in previous kinesin structures, including a fluctuating power stroke, a post-hydrolysis state bound to ADP + free Pi, and shortening of β-strands prior to Pi release and the recovery stroke. Our new findings explain the coupling between ATP binding and motor interactions with microtubules, which underlie force production by the motor and provide the basis for the enhanced mechanical output by NcdY485K compared to wild-type Ncd. The finding that the kinesin-14 working stroke fluctuates between the pre- and post-power stroke reveals an indeterminate mechanism of force generation by the motor with multiple metastable states that occur upon ATP binding. The changes we observe are variations of movements observed in other kinesin motors or affect structural elements that are highly conserved in the kinesin motors.

Results

MT-NcdY485K cryo-EM structures in three nucleotide States

We performed structural analysis on a truncated form of the NcdY485K motor (hereafter denoted NcdY485K or NcdYK) that contains the coiled-coil stalk, which dimerizes the motor and is essential for Ncd minus-end directed motility[14,21,30,31], together with the Y485K mutation[29] (Fig. 1a). The tighter microtubule binding by NcdY485K is advantageous for solving high-resolution cryo-EM structures of the motor-microtubule complex. We solved the cryo-EM structures of microtubule-bound NcdY485K (MT-NcdY485K).

NcdY485K in three different nucleotide states: (i) NF, (ii) AMP-PNP (ATP state mimic), and (iii) ADP·Pi transition state (Supplementary Table 1; Fig. 1b-d and Supplementary Fig. 1). We applied MiRPv2[32] for high-resolution analysis of 13- and 14-protofilament (PF) pseudo-helical microtubules. We obtained densities corresponding to NcdY485K in the NF, AMP-PNP, and ADP·Pi states bound to 13 PF and 14 PF MTs at 3.24 to 4.02 Å resolution (Supplementary Figs. 2 and 3, and Supplementary Table 2). Because the 14 PF maps were of higher quality, we used the 14 PF maps for the structural analysis reported here.

Although the density attributable to the NcdY485K motor domain was weaker than tubulin, we could clearly see density in each state corresponding to the MT-bound and unbound NcdY485K motor domain, or head, together with density for the coiled-coil stalk (Fig. 1b-d). Strikingly, the position of the stalk differed in each nucleotide state. The stalk was tilted towards the microtubule plus end in the NF state, it showed weak density that could be resolved into two conformations in the AMP-PNP state (see MT-NcdY485K ATP section), and it was tilted towards the microtubule minus end in the ADP·Pi state (Fig. 1b-d). We interpret the stalk in the NF state to represent the MT-bound pre-Power Stroke (PS) conformation and the stalk in the ADP·Pi state to show the MT-bound post-PS conformation (Supplementary Table 1). This interpretation is consistent with lower resolution MT-Ncd cryo-EM reconstructions (Supplementary Fig. 3)[21].

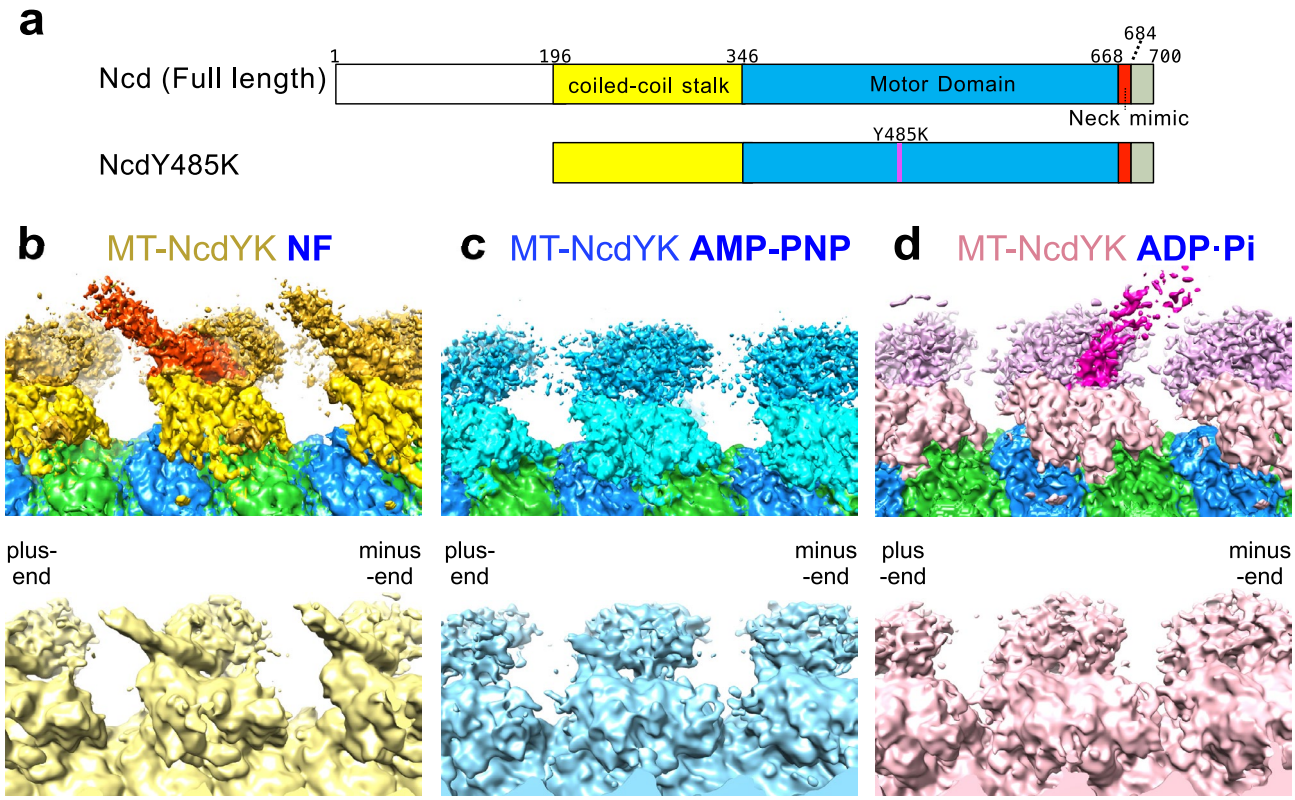

Fig. 1. Kinesin-14 Ncd domains and MT-NcdY485K cryo-EM nucleotide states. **a** Ncd domain architecture. Ncd (Full length) and NcdY485K (altered residue, magenta; analyzed in this study). The Ncd neck mimic (red) consists of residues 669 to 684 (16 aa). Stalk, yellow; motor domain, blue. **b-d** Cryo-EM density maps of NcdY485K bound to a microtubule in three nucleotide states. Top, α-tubulin is green and β-tubulin, blue. Bottom, 6 Å low pass filtered maps. The microtubule plus end is on the left and the minus end is on the right in each image. **b** MT-NcdY485K NF state. Top, the MT-bound NcdY485K head is yellow, the unbound head is dark gold, and the coiled-coil stalk is orange. **c** MT-NcdY485K AMP-PNP state. Top, the MT-bound NcdY485K head is cyan and the unbound head is dark cyan. **d** MT-Ncd Y485K ADP·Pi strong binding state. Top, the MT-bound NcdY485K head is pink, the unbound head is purple, and the stalk is magenta.

MT-NcdY485K nucleotide-free state

We built an atomic model of MT-NcdY485K in the NF state by first fitting a previously reported crystal structure of wild-type Ncd (PDB 1CZ7, dimer 2, chains C and D) into the cryo-EM map. The crystal structure shows Ncd with both heads bound to ADP, unattached to microtubules[33]. The 1CZ7 structure produced the initial MT-NcdY485K NF cryo-EM model. When fitting the motor domain of 1CZ7 chain C into the MT-bound head cryo-EM density, we found a slight tilt of the helical stalk (Fig. 2 and Supplementary Fig. 4). To further fit the stalk and unbound head, we applied a 6 Å low pass filter to the map to enhance the signal-to-noise ratio of the stalk and unbound head densities. The 1CZ7 chain D could then be rigidly fitted into the cryo-EM density corresponding to the unbound head without the tilt of the stalk, resulting in an unambiguous fit of the crystal structure into the density corresponding to the stalk and unbound head. The model was then further refined (Fig. 2).

NcdY485K in the MT-NcdY485K NF model closely resembles the wild-type Ncd 1CZ7 structure[33] (dimer 2, chains C and D; RMSD of NF bound head and chain C head for 309 paired residues from N348 to N667 is 1.094 Å) (Supplementary Fig. 4a). After alignment of the motors by the NF unbound head or 1CZ7 chain D head, the MT-NcdY485K NF bound head is displaced by ~ 7° towards the microtubule plus end compared to the 1CZ7 chain C head. By contrast, the NF unbound head and stalk are oriented the same as the crystal structure chain D (Supplementary Fig. 4a, b), implying the presence of ADP in the unbound head. The Ncd neck mimic – the C-terminal region of the kinesin-14 motors that is structurally homologous to the neck linker of kinesin-1 and other plus-end directed kinesin motor[24] – is disordered in the MT-bound NcdY485K NF cryo-EM structure and is not built into the model. Movements are also observed in the switch I/II motifs, which undergo large changes in conformation during the nucleotide hydrolysis cycle. As observed in plus-end directed kinesins[34,35], microtubule binding induces a loop-to-.

helix transition of switch II helix α4 at its N terminus. This conformational change results in the formation of an ion: dipole interaction[36] between N600 of Ncd helix α4 and E414 of α-tubulin helix H12 (Fig. 2b), which forms the initial binding interaction between the motor and tubulin. Binding by Ncd N600 to tubulin causes a mutant that converts the residue to lysine to have a strong dominant effect on microtubule binding[37]. The

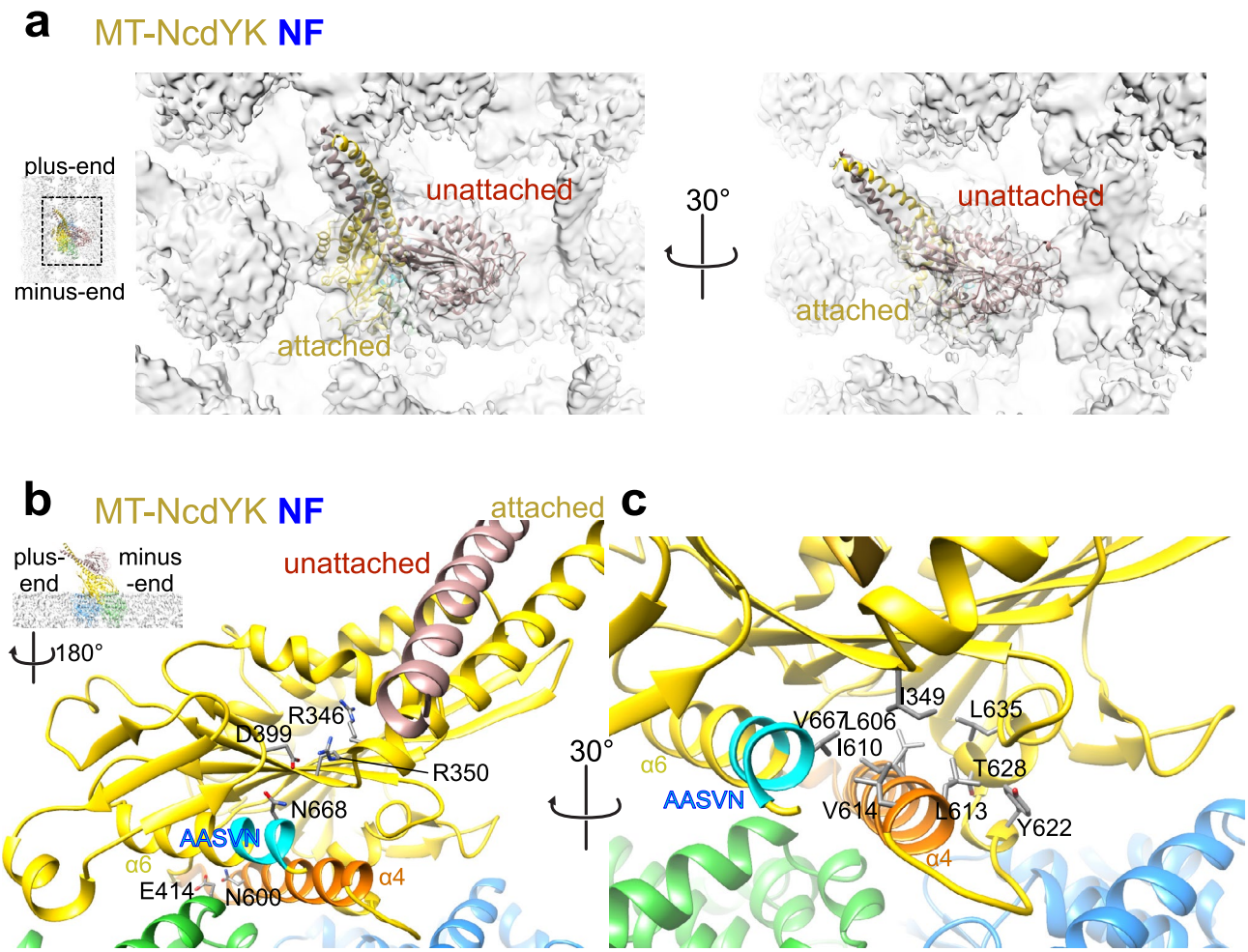

Fig. 2. MT-NcdY485K nucleotide-free state. **a** MT-NcdY485K NF cryo-EM structure. Cryo-EM density was filtered by a 6 Å low pass Gaussian filter. The MT-bound head is yellow and the unbound head is light brown. **b**, **c** Cryo-EM model of the NcdY485K bound head in the NF state. The AASVN motif at the C-terminal end of helix α6 and base of the neck mimic, which is required for Ncd minus-end motility[22,23], is colored cyan, switch II helix α4 is orange, α-tubulin is green, and β-tubulin, blue. **b** Hydrophilic or **c** hydrophobic residue interactions near switch II helix α4 and the AASVN motif, and hydrophobic side chains around the base of the stalk (stick models).

NcdN600K mutant binds 2-3x more tightly to microtubules than wild type and blocks activation of the motor ATPase by microtubules[37] – the strong ionic interactions between the mutated NcdN600K residue and α-tubulin E414 would trap the mutant motor in a nucleotide-free motor-microtubule complex. Microtubule binding also stabilizes the kinesin-14 Ncd helix α6 C-terminus at the base of the neck mimic containing the AASVN motif (residues 664–668), which is required for Ncd minus-end directed motility[22,23]. The AASVN motif forms a hydrophobic interface that includes strand β1, loop L12, and helix α4 and α5 residues (Fig. 2c). N668 is close to D399, which forms a hydrophilic interaction with V351 of strand β1, stabilizing the stalk at its base (Fig. 2b). These interactions induce a small tilt of the stalk, reducing the distance between loop L10 and the stalk (Supplementary Fig. 4b).

MT-NcdY485K ADP·Pi state

We reconstituted the ADP·Pi state by incubating NcdY485K with ADP-AlF_3 attached to microtubules and analyzed by high-resolution cryo-EM. An atomic model of MT-NcdY485K in the ADP·Pi state was built by first fitting chain B of Ncd PDB 1N6M, in which the stalk bound to head H1 of chain A is rotated towards the microtubule minus end and thought to mimic the rotated stalk after ATP binding[14–17], into the cryo-EM density of the MT-bound head. The structure of the bound head differs from Ncd PDB 1CZ7[33]. It was manually refined using a crystal structure of human kinesin-1 in the ADP·Pi state bound to α,β-tubulin (PDB 4HNA)[35] and an AlphaFold2-predicted structure[38] of full-length monomeric Ncd (AF-A0A0B4LI25-F1-model_v4.pdb) as guides (Supplementary Fig. 5). A 6 Å resolution low pass filtered electron density map was used to model the unbound head and stalk. We first rigidly fit the Ncd 1N6M chain A motor domain and stalk into the density

of the unbound head. We then tilted the stalk ~ 35°, measured from the bound head, to fit into the density and refined the model, which fit unambiguously into the density (Supplementary Fig. 5a, b).

A striking feature of the MT-NcdY485K ADP·Pi structure is that the stalk has undergone a large rotation from its position in the MT-bound NF structure (Fig. 1b-d and Supplementary Movie 1) and is tilted toward the MT minus end, positioned in the MT-bound post-PS conformation. The stalk angle of the MT-NcdY485K ADP·Pi structure differs from a Ncd crystal structure (Supplementary Fig. 5c, see below)[14,33]. When aligned by the unbound head, the MT-bound head is tilted by ~ 10° more perpendicular to the microtubule surface (Supplementary Fig. 5c, d) compared to Ncd 1N6M, which is interpreted to represent an unbound post-PS state[14].

Another striking feature of the MT-NcdY485K ADP·Pi cryo-EM structure is that the neck mimic at the C terminus of the motor is fully visible (Fig. 3 and Supplementary Fig. 5a). In the MT-NcdY485K ADP·Pi transition state cryo-EM structure, rotation of switch II helix α4 at the motor-microtubule binding interface causes the stalk rotation from the pre- to post-PS conformation altering AASVN interactions so that N668 is now close to R350, but retains its hydrophilic interactions with D399 in the loop between strands β1c and β2. N348, at the base of the stalk, has turned to face D399 and N668, and may form hydrophilic interactions through water, stabilizing the rotated stalk (Fig. 3a).

The rotated stalk in the MT-NcdY485K ADP·Pi state is stabilized by interactions of hydrophobic patches in strand β1, helix α4, and helix α6 with the neck mimic, which is docked onto the motor core along its length (Fig. 3a, b). As in the NF state, helix α6 AASVN motif residues stabilize the base of the neck mimic by hydrophobic contacts with strand β1 and helix α4 residues (Fig. 3b). Neck mimic residues R677, N678, and R679 interact with or are positioned close to helix α3 D424, loop L13 N638 and strand β7 S572, respectively, at the edge of

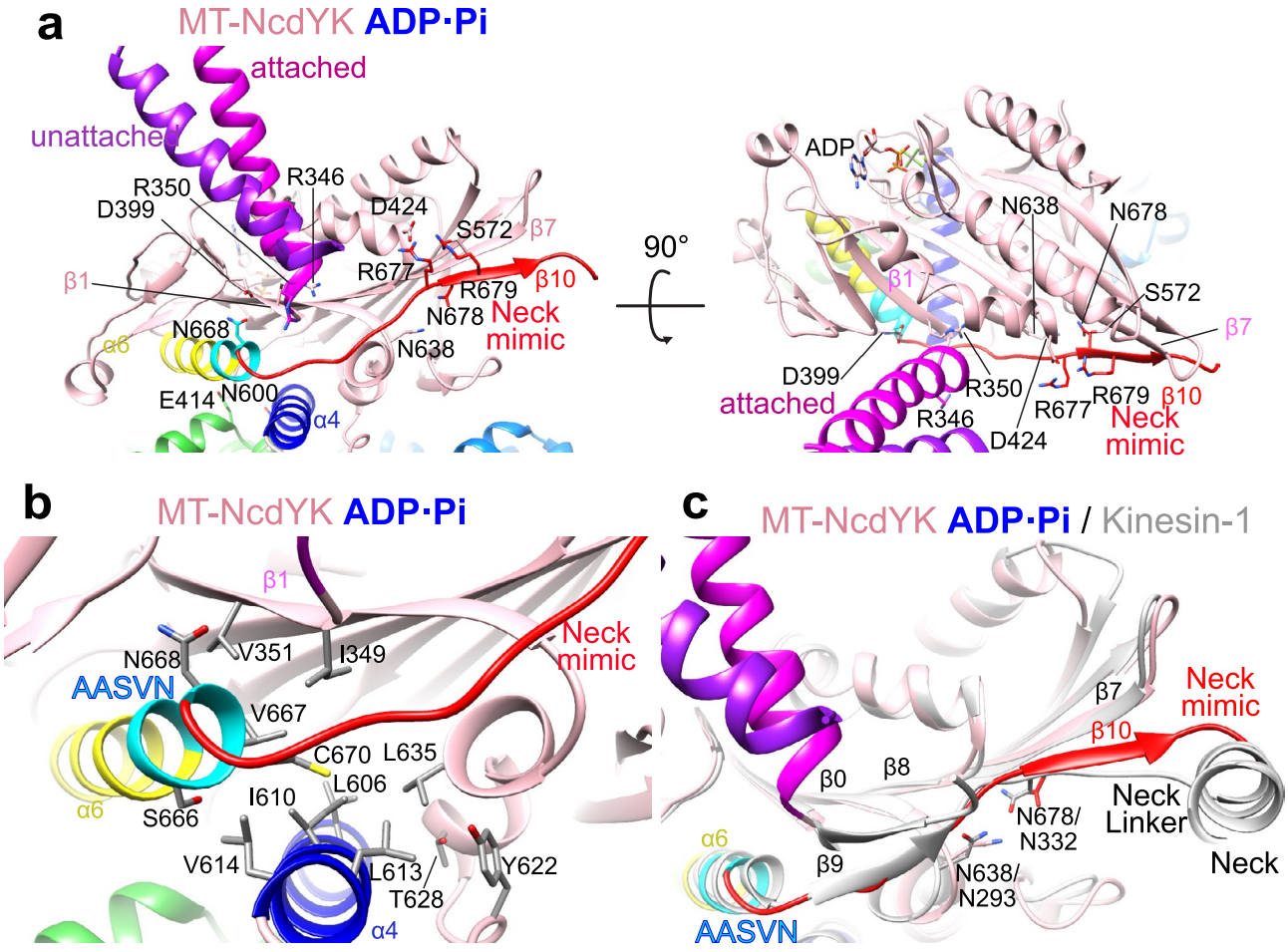

Fig. 3. MT-NcdY485K ADP·Pi state. **a** Cryo-EM structure of MT-NcdY485K (motor domain, pink) bound to an ADP·Pi transition state analogue[39]. The stalk helix of the MT-bound head is magenta and the stalk helix of the unbound head is purple. NcdY485K switch II helix α4 is dark blue, helix α6 is yellow with the AASVN motif at the C-terminus of helix α6 shown in cyan, and the neck mimic is red. α-Tubulin, green; β-tubulin, blue. **b** Hydrophobic residues around helix α4, the AASVN motif, and the base of the stalk at the motor-MT interface. **c** Superposition of the NcdY485K ADP·Pi (pink) and kinesin-1 (KIF5B, PDB 1MKJ; gray) motor domain showing the kinesin-1 two-stranded cover-neck bundle (strands β0 and β9). NcdY485K neck mimic N638 and N678 align with kinesin-1 neck linker N293 and N332, as shown.

the central β-sheet, stabilizing interactions with the motor core (Fig. 3a). The MT-NcdY485K ADP·Pi cryo-EM structure compared with a plus-end directed kinesin-1 crystal structure (PDB 1MKJ) shows that the docked neck mimic overlaps with the neck linker in position, but has different interactions with the motor core (Fig. 3c). A major difference is that the cover strand, β0, at the N-terminus of the kinesin-1 motor domain forms a small two-stranded β-sheet, the cover-neck bundle, with strand β9 of the neck linker (Fig. 3c). Kinesin-14 lacks the cover strand and the cover-neck bundle, thus docking of the neck mimic onto the motor core is likely to produce less force than docking of the neck linker, although the initial region of the neck mimic stabilizes the stalk at its base by forming a shallow hydrophobic pocket (Fig. 3b, c). Moreover, β10 of both the NcdY485K neck mimic and kinesin-1 neck linker form H-bonds to β7 of the central β-sheet, extending the β-sheet (Fig. 3c and Supplementary Movie 2) and altering its structure (Supplementary Table 3). Further, residues in the middle of the NcdY485K neck mimic (N678) and kinesin-1 neck linker (N332 in 1MKJ) both interact with loop L13 of the LGGN motif (N638 in Ncd or N293 in kinesin-1; Fig. 3a, c), which is conserved in the kinesin superfamily proteins[40].

We also analyzed the changes in NcdY485K electrostatic potential upon neck mimic docking. Before neck mimic docking, the surface of the region involved in docking is negatively charged (Supplementary Fig. 5e, red-filled dashed circle). After docking, the neck mimic covers the negatively charged surface and converts it to a positive charge (Supplementary Fig. 5f, blue-filled dashed circle). Charge repulsion and steric clashes of side chain residues between the stalk and the neck mimic would drive the stalk from the pre-PS position, inducing stalk rotation to the post-PS position. The MT-NcdY485K ADP·Pi structure shows not only that the neck mimic resembles the docked neck linker of plus-end directed kinesin-1[11,41] but that it induces rotation of the stalk and is docked onto the edge of the central β-sheet following the power stroke, distorting the β-sheet (Supplementary Table 3).

MT-NcdY485K ATP state

For the MT-NcdY485K AMP-PNP cryo-EM map, no model exists, including from previously reported crystal structures. We initially fit our MT-NcdY485K NF and ADP·Pi cryo-EM models into the density (Supplementary Fig. 6). For the MT-NcdY485K AMP-PNP density corresponding to the attached head, the MT-NcdY485K NF and ADP·Pi bound heads appeared at first glance to fit. However, careful examination of the MT-NcdY485K AMP-PNP density map revealed that structural elements were mismatched in the fits with both models (Supplementary Fig. 7). Ambiguities in the MT-NcdY485K AMP-PNP cryo-EM map were also evident from the finding of two regions of density corresponding to the base of the stalk (Supplementary Fig. 6 and Supplementary Fig. 7). This was attributed to conformations of the MT-bound head in two or more metastable states, including the pre- and post-PS states. To classify these states, we applied 3D-focused classification, but the attempt failed. This suggests that the NcdY485K AMP-PNP state fluctuates between multiple indistinguishable states. The finding of two regions of density for the base of the stalk in the MT-NcdY485K AMP-PNP cryo-EM map implies that the stalk fluctuates between the pre-PS and post-PS positions when the MT-bound head binds to ATP (Supplementary Fig. 6a). This interpretation is consistent with lower resolution cryo-EM structures of Ncd bound to the ATP analogue, AMP-PNP, in which density attributed to the stalk is weak or not visible[21,42], compared to Ncd with no nucleotide or bound to ADP·Pi.

A comparison of the cryo-EM density corresponding to the unbound head of the MT-NcdY485K AMP-PNP, MT-NcdY485K NF, and MT-NcdY485K ADP·Pi structures is also consistent with fluctuations between pre- and post-PS states by the MT-NcdY485K AMP-PNP bound head. The density corresponding to the unbound head of the MT-NcdY485K AMP-PNP structure is not in the same position as the unbound head of the MT-NcdY485K NF or ADP·Pi models (Supplementary Fig. 6a, b). The MT-NcdY485K NF cryo-EM map shows density between the unbound head and the microtubule surface (Supplementary Fig. 6b, arrows), which is not observed in the MT-NcdY485K AMP-PNP cryo-EM map; rotation of the unbound NF head is also required to fill the density. The shape of the density for the unbound head in the ATP state is similar to that in the ADP·Pi state, but the unbound head density in the ATP state is displaced towards the MT plus end compared to the ADP·Pi state. These results imply that the MT-NcdY485K AMP-PNP bound head fluctuates between multiple metastable states that are similar to the more stable MT-NcdY485K NF and MT-NcdY485K ADP·Pi pre- and post-PS states, respectively.

Neck mimic binding precedes the kinesin-14 power stroke

Our analyses elucidated the structural transition from the NF to the ADP·Pi (ADP-AlF_3) state, which includes ATP binding and isomerization. This transition involves two mechanical steps: the docking of the neck mimic to the motor domain and the rotation of the stalk to produce the power stroke. In the ATP-bound AMP-PNP state, the motor fluctuates between the NF and ADP·Pi states. Because of the fluctuations, the causal relationship and sequence of events, in which ATP binding, neck mimic docking, and stalk rotation occur, remain unclear. To address this, we used molecular dynamics (MD) simulations to investigate the mechanism for the transition from the NF to the ADP·Pi state.

In the simulations, we used a coarse-grained (CG) model that reduces the computational time by representing each amino acid as a single bead (Fig. 4a, Supplementary Fig. 8a)[43]. We then performed MD simulations using two protocols to study molecular mechanisms for the transition from the NF to the ADP·Pi state. We first examined the structural fluctuations around the cryo-EM structures of the NF and ADP·Pi states using equilibrium MD simulations (Fig. 4b). We then used the *Switching Gō* algorithm in the MD simulations[44], where we induced a one-time transition from NF to ADP·Pi, mimicking ATP hydrolysis, and analyzed the structural response (Fig. 4b). Both simulations were conducted in the presence and absence of the neck-mimic, allowing us to investigate its role in the transition. To quantify the conformational change, we defined two angles, θ and φ, that characterize the orientation of the stalk relative to the microtubule (Fig. 4c). We performed 100 simulations

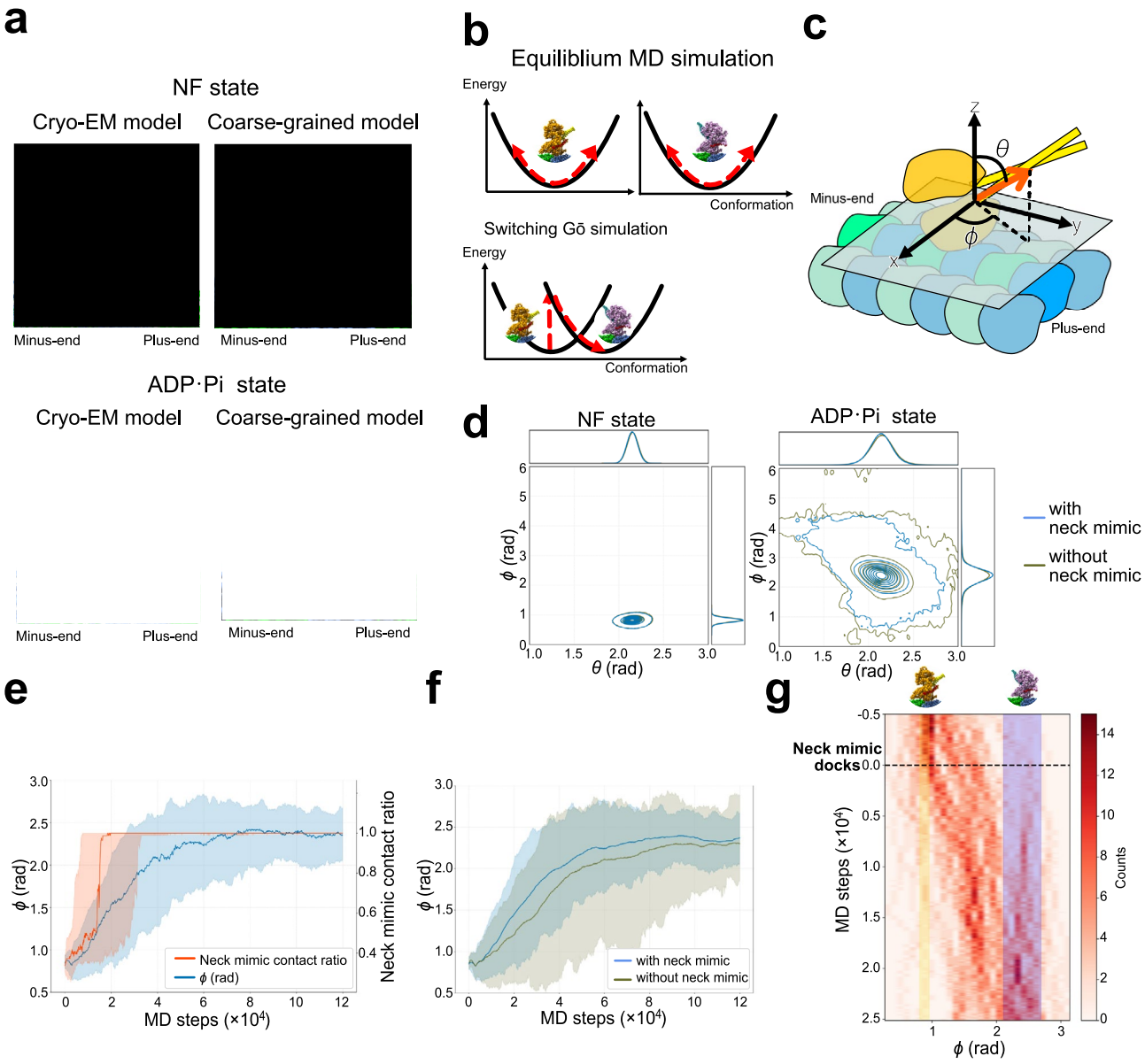

Fig. 4. MD simulation of NcdY485K. **a** Cryo-EM and coarse-grained models of the NF state (stalk, yellow; motor domains, orange) and ADP·Pi (ADP-AlF_3) state (stalk, purple; motor domains, pale purple). Neck mimic, red; α-tubulin, green; β-tubulin, blue. **b** Equilibrium MD simulations performed using state-specific, structure-based force fields. **c** Simulation parameters: axes, plane and angles (θ , φ). **d** Distributions of angles (θ , φ) in NF and ADP·Pi MD equilibrium simulations with (blue) or without the neck mimic (blue-green). Radian, rad. **e***Switching Gō* simulation neck mimic contact ratio (Right axis, median, red line) and angle φ (Left axis, median, blue line). Red or blue shading, 80% of data. **f***Switching Gō* simulation angle φ for ADP·Pi with (blue) or without (green) the neck mimic. Blue or green shading, 80% of data. **g***Switching Gō* simulation distributions of angle φ (red) with neck mimic docking defined as time 0. Yellow (NF) or purple (ADP·Pi) shading, mean ± 1 SD.

for each condition. For the equilibrium MD simulations, the number of MD steps was set to 1.0×10^7, while for the *Switching Gō* simulations, it was set to 2.0×10^6 (Supplementary Table 4).

Equilibrium MD simulations of the NF and ADP·Pi states revealed differences in the structural stability of the stalk region. In the NF state, the stalk position converged to that observed in the NF cryo-EM structure. By contrast, the ADP·Pi state exhibited greater fluctuations of the stalk around its cryo-EM structure (Fig. 4d, Supplementary Fig. 8b). Furthermore, the ADP·Pi simulations without the neck mimic showed even larger fluctuations of the stalk compared to those that included the neck mimic.

In *Switching Gō* simulations, after the neck mimic residues K671 to K676 converged into the ADP·Pi position, interactions with other regions were rapidly induced, leading to a fully and stably docked neck mimic onto the motor domain (Fig. 4e, Supplementary Fig. 8c). Upon binding, the neck mimic conformation was essentially

unchanged. By contrast, the stalk exhibited a back-and-forth swinging motion before stabilizing in the ADP·Pi state (Fig. 4e).

To further investigate its role, we compared MD simulations with and without the neck mimic (Fig. 4f, Supplementary Fig. 8d). Models with the neck mimic transitioned to the ADP·Pi state more rapidly than those without it. Moreover, the presence of the neck mimic reduced the stalk fluctuations in the ADP·Pi state, consistent with the equilibrium MD simulation results (Fig. 4d). Lastly, to better characterize the transition, we defined neck mimic docking onto the motor domain as time zero (Fig. 4g). At the time of docking, only 9.2% of simulations exhibited stalk swinging toward the ADP·Pi state. Instead, the stalk transitioned gradually over the subsequent 100–200 MD steps before stabilizing in the ADP·Pi position.

These findings imply that the transition of the stalk position from the NF to the ADP·Pi state follows binding of the neck mimic. This stepwise transition provides insight into the molecular mechanism underlying the power stroke in kinesin-14 – it emphasizes the role of the neck mimic in effecting ATP binding-driven conformational changes of Ncd.

NcdY485K crystal structure bound to free Pi with docked neck mimic

The NcdY485K dimeric motor was crystallized in the presence of excess Pi, and the structure was solved by molecular replacement (Supplementary Table 5). The 3.15 Å resolution model shows new structural features of the Ncd motor following ATP hydrolysis and motor detachment from the microtubule. The NcdY485K heads are oriented differently from one another in the crystal structure (Fig. 5), indicating that they represent different states of the mechanochemical cycle. Head H1 resembles previous crystal structures of wild-type Ncd bound to ADP (e.g., PDB 1CZ7), which show extensive interactions of the two heads with the end of the stalk. In the NcdY485K crystal structure, the stalk retains its interactions with head H1 but has undergone a large rotation of ~ 80°, reorienting the stalk and head H1 relative to head H2 (Fig. 5a), as in other Ncd wild-type and variant or mutant crystal structures[14–17]. Both heads contain density corresponding to ADP bound to the active site, but the head H2 active site also contains density for Pi adjacent to the bound nucleotide (Fig. 5a). Density for Mg^{2+}, which is ~ 4-fold smaller in mass than Pi, could not be identified with certainty. Strikingly, the neck mimic is visible in head H2 (Fig. 5b, c and Supplementary Fig. 9a), unlike previously reported Ncd crystal structures, where the neck mimic is disordered and not visible[14–17]. We interpret head H1 of the NcdY485K crystal structure to represent a MT-unattached pre-PS state and head H2 to reveal a previously unreported MT-detached post-PS state (Supplementary Fig. 9b-e).

Several differences exist between head H2 of the crystal structure and the bound head of the MT-NcdY485K ADP·Pi cryo-EM structure, which represent different post-PS states. First, switch II helix α4 in head H2 of the crystal structure has undergone a helix-to-loop transition, shortening the structured region of the helix (L603-L614, 12 aa) by > 50% at both its N- and C-termini relative to the MT-NcdY485K ADP·Pi bound head (R592-K616, 25 aa) (Supplementary Fig. 9a), as well as other MT-bound or unbound kinesin motors, including plus-end directed kinesins[45,46]. However, the tilt of helix α4 in head H2 of the crystal structure is similar to that of the MT-NcdY485K ADP·Pi bound head (Supplementary Fig. 9a), implying that the nucleotide state of head H2 is close to that of the MT-bound motor after microtubule detachment. The neck mimic in head H2 of the crystal structure (S669-Y680, 12 of 16 neck mimic residues) is visible and docked onto the motor core. The head H2 neck mimic and docked neck mimic in the MT-NcdY485K ADP·Pi bound head (C670-S684) differ in length and also by the inclusion of a residue, S669, that is present in helix α6 of the MT-NcdY485K ADP·Pi bound head. This residue has unwound to form the first residue of the neck mimic in head H2 of the crystal structure. Ncd neck mimic strand β10, which forms hydrogen bonds with the end of β7 in the ADP·Pi bound head, is unstructured or disordered in head H2 of the NcdY485K crystal structure (Supplementary Fig. 9a). Further, the neck-mimic in head H2 of the crystal structure has a high B-factor compared to other regions of the motor that include head H1 and the stalk (Fig. 5c). The structural elements at the head H2 motor-microtubule binding interface also show high B-factors, including strand β4 and/or loop L7 – the site of the NcdY485K mutation – and L11. Nonetheless, these regions are well defined in the electron density map. The high B-factors of these structural elements indicate increased flexibility accompanying motor detachment from the microtubule.

NcdY485K central β-sheet twisting and strand-to-loop transitions

The NcdY485K crystal structure further shows large changes in the central β-sheet of head H2 compared to head H1, which are also observed in the MT-NcdY485K NF and MT-NcdY485K ADP·Pi bound heads (Fig. 6, Supplementary Tables 3 and Supplementary Movies 3–5) and unbound heads (Supplementary Table 3). The central β-sheet of the kinesin motors is evolutionarily conserved with myosin[5]. In myosin, twisting or distortional movements of the β-sheet have been proposed to close the major 50 kDa cleft, driving ADP release and the swing of the lever arm during the power stroke[26,27]. The myosin β-strands that undergo the largest distortional changes between nucleotide states are strands 5–7, which precede the switch II loop, follow switch I, or are adjacent to switch I. Myosin strands 5–7 correspond to kinesin strands β7, β6, and β4, respectively[28]. Residues in these three strands of NcdY485K head H2 show large changes in side chain position and orientation compared to head H1 (Fig. 6d, e). The movements are especially pronounced at the ends of strand β4 and involve W473 which is at the N terminus of β4 or present in the adjacent loop L6, depending on the nucleotide state (Fig. 6c-e and Supplementary Fig. 9b-e), and the Y485K residue at the C terminus of β4 or in loop L7 (Fig. 6d, e) near the motor-microtubule binding interface. W473 is close to loop L10, which interacts with the stalk in the unbound and MT-bound pre-PS states (Supplementary Fig. 9d). The β-sheet twisting is first observed in the MT-NcdY485K NF state (Supplementary Table 3, Fig. 6b and Supplementary Movie 4) and is increased in the MT-NcdY485K ADP·Pi bound head following the power stroke (Supplementary Table 3, Fig. 6c, Supplementary Movies 1 and 5), and in NcdY485K head H2 after release from the MT (Supplementary Table 3), implicating

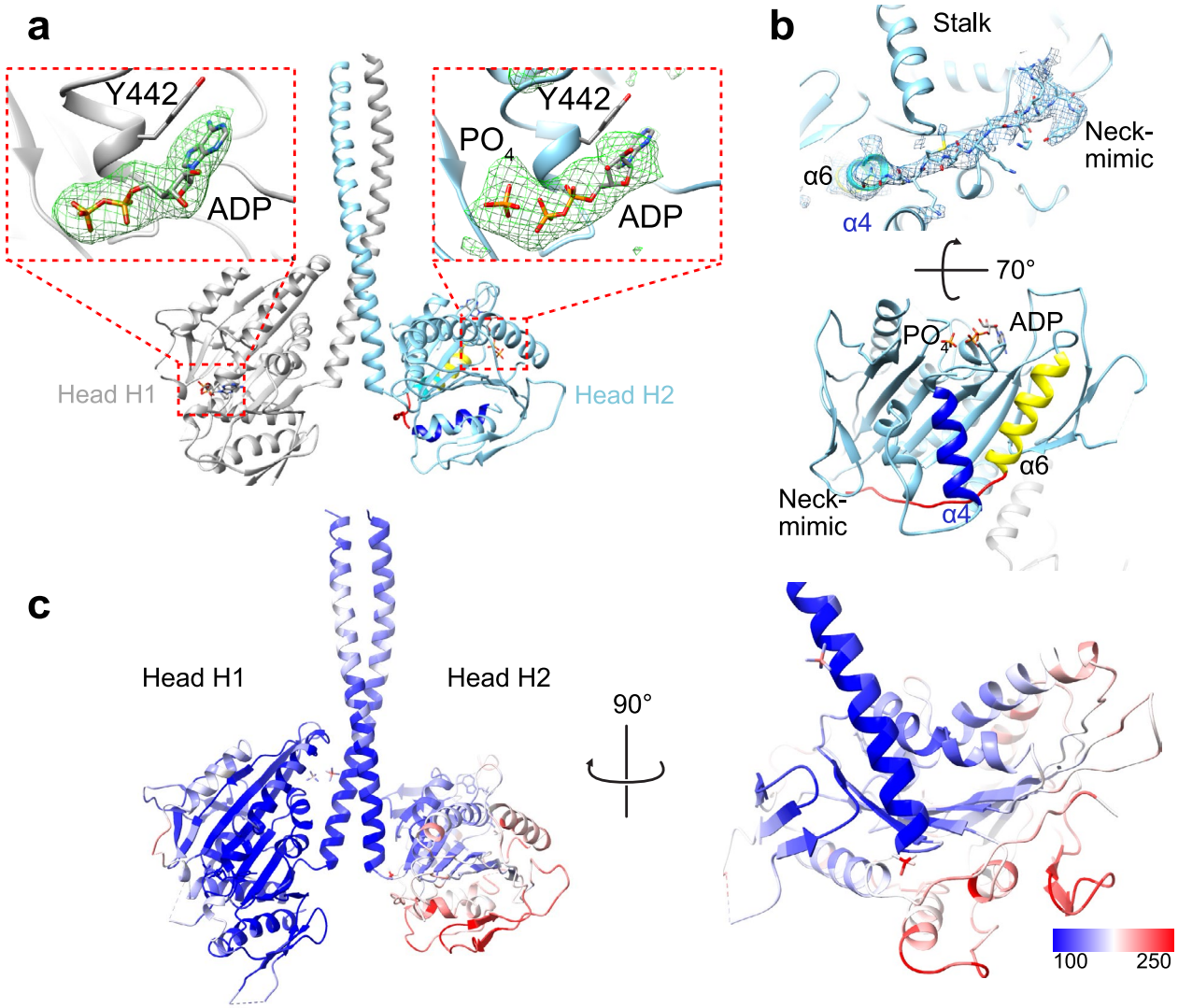

Fig. 5. NcdY485K crystal structure in MT-unattached post-PS state. **a** NcdY485K crystallized in the presence of high Pi concentration. Head H1 (chain A) is gray, and head H2 (chain B) is light blue. Insets, head H1 (left) and H2 (right) active sites showing Fo-Fc difference maps (green mesh) of the bound nucleotide with ADP or ADP + free Pi (stick models), respectively, built into the density. Maps contoured at 2.5 σ. The adenine ring of the bound ADP shows ring-stacking interactions with Y442 of the P loop at the nucleotide-binding cleft in both heads. **b** Neck mimic in head H2. Top, 2Fo-Fc difference map (blue mesh) showing density for head H2 neck mimic (stick models) contoured to 0.8 σ. Bottom, view from head H2 MT-binding surface. Neck mimic, red; switch II helix α4, dark blue; helix α6, yellow with AASVN in cyan. **c** NcdY485K crystal structure colored by B-factor. Scale bar, B-factor range = 100–250 Å^2.

β-sheet distortional changes in triggering stalk movements in kinesin-14 that produce force and displacements along microtubules.

In addition to the twisting of strands in the central β-sheet, extensive changes in the lengths of strands β4, β6, and β7 are observed between head H1 and H2 of the NcdY485K crystal structure (Fig. 6a and Supplementary Table 6) that are caused by the conversion of the β-strands in head H2 into loops. Differences in β-strand length are also observed between head H1 and H2 of previous Ncd crystal structures (Supplementary Table 6), as well as between head H2 of the crystal structure and the MT-NcdY485K NF or ADP·Pi bound head, both of which have longer β-strands than either head H2 (Fig. 6a) or H1 (Fig. 6b, c). The differences in β-strand length between head H1 and H2 of the previous Ncd crystal structures could be due to differences in the post-PS transition states that the structures represent, some of which may correspond to states after Pi release. The strand-to-loop transitions in NcdY485K head H2 reduce the lengths of β4, β6, and β7 by as much as ~40–70%, compared to head H1 or the MT-NcdY485K NF and ADP·Pi bound heads. The NcdY485K head H2 central β-sheet has higher B-factors (C_a, 99.6 to 167.8 Å^2) compared to head H1 (C_a, 65.5 to 120.5 Å^2) (Fig. 5c), evidence of increased flexibility of the head H2 central β-sheet. We hypothesized that the head H2 strand-to-loop transitions are induced by ADP + free

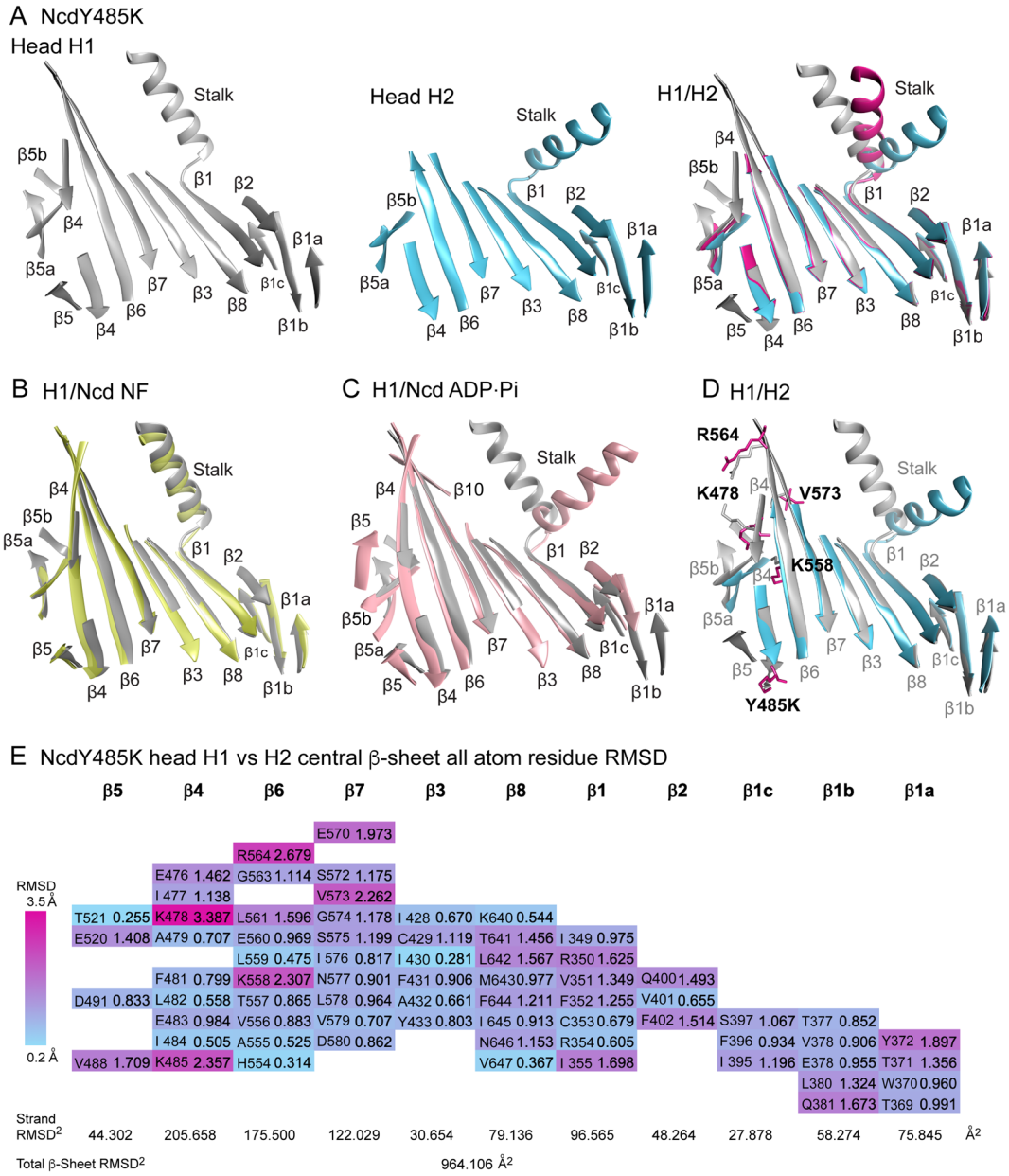

Fig. 6. NcdY485K central β-sheet twisting or distortion. **a** NcdY485K crystal structure central β-sheet, including strands β1a, b,c and β5a, b. Left, NcdY485K head H1 ADP (gray, pre-PS). Middle, NcdY485K head H2 ADP + free Pi (cyan, post-PS). Right, images from morph between H1 and H2 (Chimera *Morph Conformation*; see Supplementary Movie 3) showing β-strand twisting and length changes between the two nucleotide states (dark red, transition). **b** NcdY485K central β-sheet movements following microtubule binding and **c** the power stroke. **b** Superposition of unbound (NcdY485K crystal structure H1, gray) and MT-bound (MT-NcdY485K NF, yellow) pre-PS heads (Supplementary Movie 4). **c** Superposition of unbound (NcdY485K crystal structure H1, gray) and MT-bound post-PS (MT-NcdY485K ADP·Pi, pink) heads (Supplementary Movie 5). **d** NcdY485K β-sheet residues (dark red, stick models, bold labels) that undergo the largest movements (> 2 Å) between NcdY485K head H1 ADP (pre-PS) and head H2 ADP + free Pi (post-PS) (Supplementary Movie 3). **e** Heat map showing NcdY485K head H1 vs. H2 central β-sheet residue all-atom RMSD values. Left, scale bar (0.2–3.5 Å RMSD). Bottom, total β-strand and β-sheet RMSD^2 (sum of squares) values. NcdY485K head H1 vs. H2 mean β-strand RMSD = 1.250±0.230 Å (mean±SD, n = 11 β-strands). By contrast, wild-type Ncd 1CZ7 dimer 2 (chain C vs. D) heads, both in the ADP pre-PS state, showed a mean β-strand RMSD = 0.342±0.082 Å (n = 11 β-strands), differing significantly from NcdY485K (P < 0.0001, unpaired t test).

Pi bound to the head H2 active site after ATP hydrolysis that causes structural changes associated with motor detachment from the microtubule.

We tested this hypothesis by adding excess Pi to NcdY485K, which is assumed to be bound to 1:1 molar amounts of ADP after purification[47], and measuring changes in NcdY485K intrinsic fluorescence produced by tryptophan (Trp) residues to detect β-sheet conformational changes. The NcdY485K dimer construct that we analyzed (Fig. 1a) contains two Trp residues in each chain, both present in strands of the central β-sheet: W370 in strand β1a is pointed inward and protected from solvent in NcdY485K heads H1 and H2, and W473 is buried in head H1 under the ends of strands β6 and β7, and adjacent L6 and L10 residues (Fig. 7a). By contrast, W473 in head H2 is exposed to solvent by the strand-to-loop transitions of β6 and β7, and of β4 adjacent to W473 (Fig. 7a). Fluorimeter assays showed overlapping excitation spectra for NcdY485K (Ex_{Max}, 275±4 nm, mean±SD, n = 4) and free Trp (274±1 nm, n = 3; P = 0.9850, unpaired t test), but emission spectra showed a shift to shorter wavelength by ~ 25 nm for NcdY485K (Em_{Max}, 333±3 nm, n = 14) compared to free Trp (357±2 nm, n = 20; P < 0.0001) (Fig. 7b and Supplementary Fig. 10a, b). The blue-shifted NcdY485K emission spectrum is consistent with greater protection of the Trp residues from solvent in the motor relative to free Trp[48]. Moreover, the addition of excess Pi to the NcdY485K motor caused a ~ 22% reduction in fluorescence, compared to ~ 7% for free Trp (Fig. 7c), consistent with an increase in Trp solvent exposure in the NcdY485K motor with Pi. Despite the reduction in fluorescence, the added Pi did not cause a shift in the NcdY485K Em_{Max} spectrum (Supplementary Fig. 10a, b). The ~ 3-fold greater fluorescence decrease following addition of Pi to NcdY485K compared to free Trp is highly statistically significant (P = 0.005, one-way ANOVA with post-hoc Tukey HSD tests).

Without excess Pi, the active site of both NcdY485K heads is expected to be bound to ADP, like head H1 of the crystal structure, with the overall NcdY485K structure resembling wild-type Ncd ADP-bound pre-PS structures (e.g., PDB 1CZ7). Upon binding to Pi, head H2 is expected to undergo structural changes resembling the

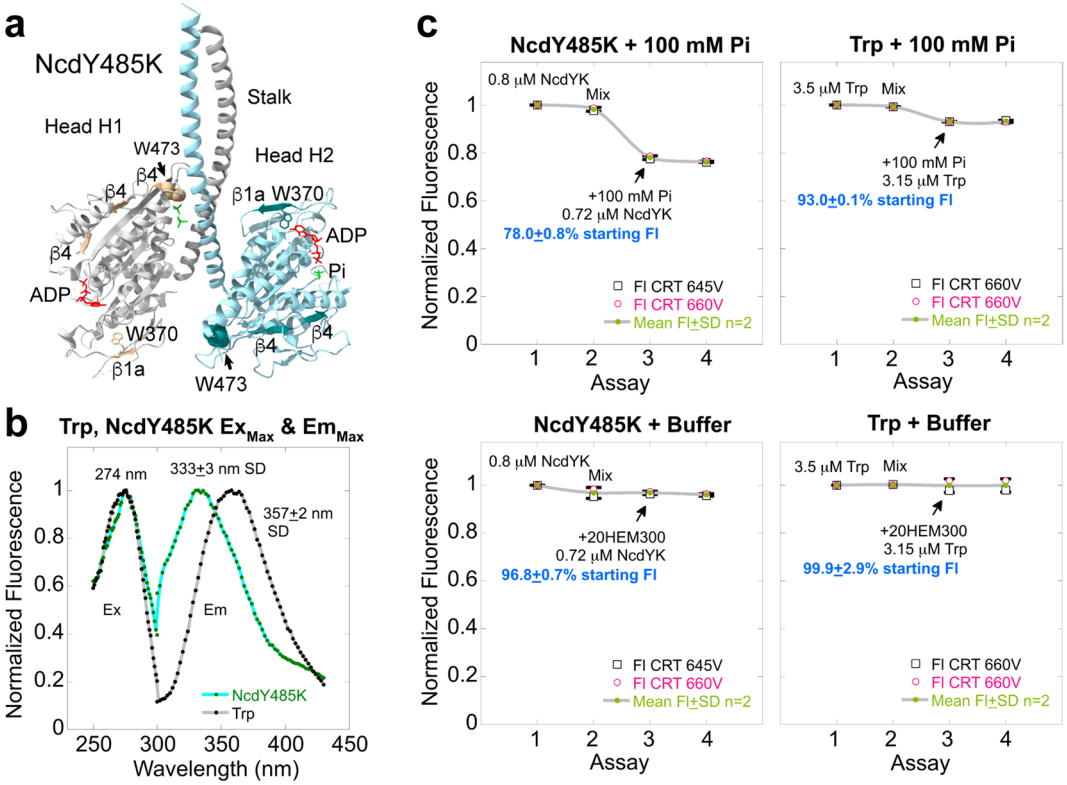

Fig. 7. NcdY485K intrinsic fluorescence assays to detect central β-sheet conformational changes. **a** NcdY485K residues W370 (yellow, stick model) and W473 (dark yellow, space filled) in head H1 (white), and W370 (cyan, stick model) and W473 (dark cyan, space filled) in head H2. **b** Free tryptophan (Trp, gray) and NcdY485K intrinsic fluorescence (cyan) excitation and emission spectra. The NcdY485K emission spectrum is blue-shifted by ~ 25 nm relative to the free Trp spectrum, indicating that the NcdY485K Trp residues are relatively buried. Ex, Excitation; Em, emission; Max, Maximum. **c** NcdY485K fluorescence assays. Top, NcdY485K (left) or free Trp (right) assays, consisting of an initial fluorescence scan followed by a scan to control for mixing effects and two scans after adding 100 mM NaPi (Na_2HPO_4/KH_2PO_4). Bottom, NcdY485K (left) or free Trp (right) assays in which the same volume of buffer was added instead of NaPi. Plots show the mean ± SD for assays performed under identical conditions of slit width, averaging time, and assay time. Data for NcdY485K are from paired buffer control assays performed at the same photomultiplier tube (PMT) voltage (V), which was close to or the same as the free Trp assays. Free Trp assays shown were performed at the same PMT V. Fl, fluorescence. CRT, all assays were corrected for dilution due to addition of NaPi or buffer, and for photobleaching (see Supplementary Fig. 10c).

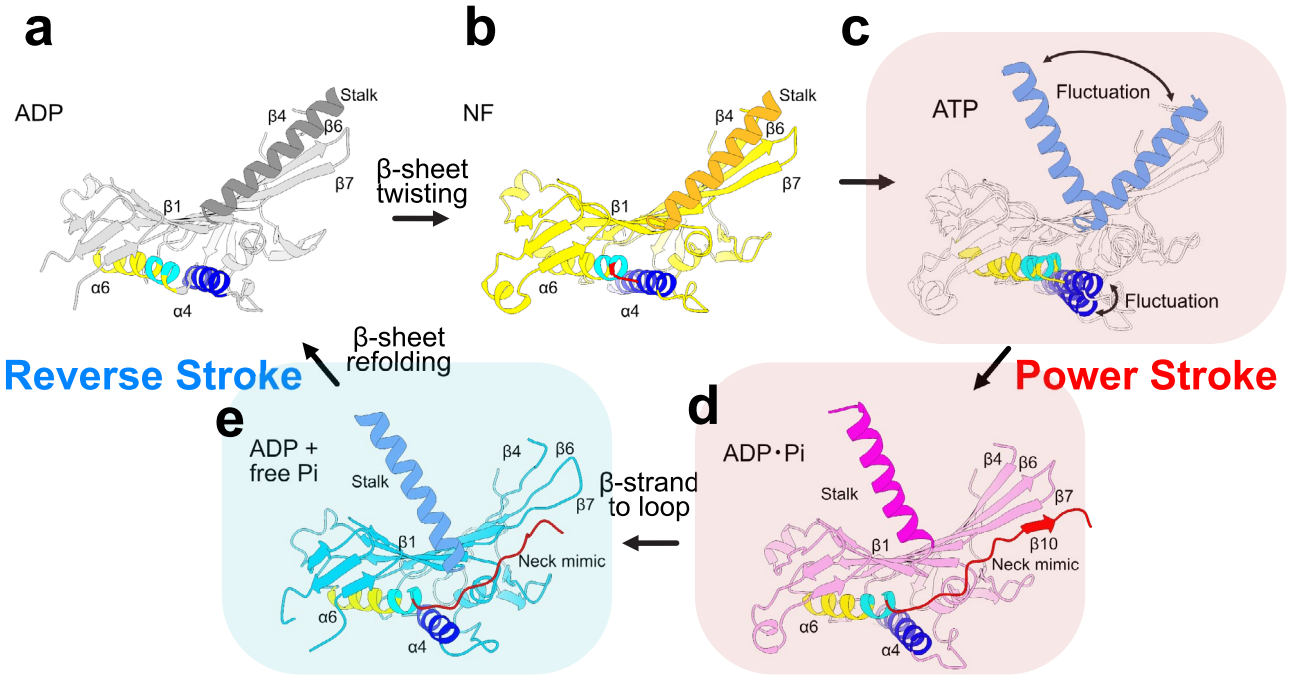

Fig. 8. Model for kinesin-14 motility. Steps of ADP release, ATP binding and hydrolysis, and Pi release for a kinesin-14 minus-end microtubule motor: **a** ADP state (unbound), **b** NF state (MT-bound), **c** ATP state (fluctuating, MT-bound), **d** ADP·Pi state (MT-bound), **e** ADP + free Pi state (unbound) (Supplementary Table 1). Following Pi release, the motor undergoes a recovery stroke to return to the ADP state (Supplementary Movie 6). Stalk helix angle changes (Supplementary Fig. 11) are shown for each state.

NcdY485K post-PS crystal structure, including β-strand to loops transitions that expose W473 to solvent, which is expected to decrease motor intrinsic fluorescence[48]. We interpret the decrease in NcdY485K fluorescence observed in the fluorimeter assays upon addition of Pi to be caused by Pi binding to the active site of head H2, inducing β-strand transitions to loops in the head H2 central β-sheet. A potential effect of the strand-to-loop conversions, together with the central β-sheet strand twisting (Fig. 6), is the storing of free energy to drive Pi release and the motor recovery stroke.

Discussion

Kinesin power stroke and recovery stroke

We report new structures that show five different MT-bound and unbound states of the kinesin-14 NcdY485K motor before, during, and after the power stroke (Supplementary Table 1). Although the ADP state (NcdY485K crystal structure head H1) is the same conformation as a previously reported wild-type Ncd motor bound to ADP[33] and we could not build a MT-NcdY485K AMP-PNP atomic model because of the fluctuations between pre-PS and post-PS states, the new structures reveal previously unreported features of the conformational changes by a kinesin motor during the motor mechanochemical cycle. These features provide new insights into the mechanism of motor energy transduction (Fig. 8 and Supplementary Movie 6).

Prior to microtubule binding, the kinesin motor, free in solution, has ADP bound to the active site[47] (Fig. 8a). The motor binds to a microtubule by one head, releasing ADP from the bound head[49] (Fig. 8b). Helix α6, which contains the AASVN motif required for kinesin minus-end motility[22,23], interacts with strand β1 and helix α4, tilting the stalk towards the microtubule plus end, stabilized by loop L6 and L10 interactions. The MT-bound head binds to ATP, causing the stalk to fluctuate in rotating towards the microtubule plus and minus ends (Fig. 8c). After ATP binding and hydrolysis, the stalk is preferentially rotated towards the microtubule minus end (Fig. 8d), consistent with our ADP·Pi cryo-EM model and a previous report[21]. Notably, the motor–microtubule interface exhibits elevated B-factors for the neck mimic and switch I/II, and the central sheet shows marked shortening of strands β4, β6, and β7, indicative of a more flexible interface. Switch I is close to the position in the bound head that is occupied by γ-phosphate, and the neck mimic is docked onto the motor core at the edge of the central β-sheet. Neck mimic docking occurs with tilting of switch II helix α4 and the C-terminus of helix α6, reminiscent of helix α4 and α6 movements upon docking of the kinesin-1 neck linker onto the motor core[34,35]. Detachment of the motor occurs with bound ADP + free Pi[50], the stalk rotated towards the microtubule minus end, and the neck mimic docked (Fig. 8e). The tilt of helix α4 in the H2 head closely matches that observed in the MT-NcdY485K ADP·Pi–bound head – together with the elevated B-factors and β4/β6/β7 strand shortening, this provides a structural rationale for weakened coupling and motor release from the microtubule. Pi release, together with structural changes that untwist and refold the central β-sheet, returns the microtubule-detached motor to the ADP state, repriming the motor for the next cycle of microtubule binding and nucleotide hydrolysis.

The NcdY485K motor reported here differs from wild-type kinesin-14 Ncd by a single amino acid residue that increases motor binding interactions with switch I, a structural motif that undergoes large changes in conformation during ATP hydrolysis, compared to wild-type Ncd. The binding by Y485K to switch I destabilizes coordination of the bound ADP by switch I, and, at the same time, stabilizes microtubule binding, increasing motor affinity for microtubules (Supplementary Fig. 12). The destabilized ADP binding by the motor increases the rate of ATP hydrolysis, which is rate-limited by ADP release, increasing motor gliding velocity on microtubules[29]. These effects explain the faster ATP hydrolysis by NcdY485K compared to wild type as an effect of the residue change on transition rates between steps (as in a Markov chain) without changing the steps in the motor mechanochemical cycle. The overall effect is an increase in motor mechanical output. The reciprocal effects[29] on ADP and microtubule binding imply that Y485 acts to couple motor nucleotide and microtubule binding by its binding interactions with switch I residues that affect motor interactions with switch II. This is also likely to be true for other kinesins, given that the Y485 residue is invariant in the kinesin motors.

Kinesin-14 power stroke fluctuations

Upon structural analysis of the NcdY485K mutant, we observed nucleotide-dependent fluctuations of the neck mimic and stalk between the pre- and post-power stroke states in the motor bound to AMP-PNP. By contrast, in the ADP·Pi state, the neck mimic and stalk are stabilized in the post–power-stroke conformation. Nucleotide-dependent structural flexibility of the stalk of wild-type Ncd bound to AMP-PNP was reported previously in lower-resolution cryo-EM maps[21,42], indicating that our observations are unlikely to be caused by the NcdY485K mutation. In plus-end-directed kinesins, the AMP-PNP-bound state shows the neck linker fully docked onto the motor core[41,46,51]. Note that the power strokes of myosin[19] and dynein[52] are also thought to occur by a multistate process (Supplementary Table S7), which may involve power stroke fluctuations upon ATP binding with transitions through multiple stable states, characteristic of a biological switch[53]. Thus, fluctuations during the power stroke may be common to motors other than kinesin-14.

The fluctuations show that the helical stalk rotates alternately towards the microtubule plus and minus end during the power stroke. The reversals in stalk rotation explain the plus-end directed displacements by a bidirectional kinesin-14 Ncd motor, which were also observed for wild-type Ncd and inferred to be due to movements of the stalk[20]. The fluctuating stalk movements indicate that the kinesin-14 power stroke is indeterminate, relying on concerted movements of other structural elements, such as the neck mimic (see below) to produce a working stroke of the motor. The fluctuations could also explain the effects of the *Aspergillus* kinesin-14 microtubule-binding tail on motor directionality as constraining effects by the tail on stalk rotation conferred by specific motility assay geometries[54]. Finally, the fluctuating power stroke provides an evolutionary link to the plus-end movement of kinesin-1, as well as other motor proteins, in which ATP binding or the power stroke may also occur in multiple metastable states (Supplementary Table 7), by demonstrating that the kinesin-14 stalk rotation can occur in either direction, directing the motor towards either the microtubule plus or minus end.

Kinesin-14 neck mimic and force production

Docking of the neck mimic along the motor core was reported previously for a kinesin-14 plant kinesin, KCBP, where a truncated, monomeric motor construct bound to Mg^{2+}-ADP was crystallized in a form interpreted to represent the motor in an ATP state[24]. The KCBP helix α6-neck mimic junction sequence more closely resembles the kinesin-1 neck linker sequence than the neck mimic of other kinesin-14 proteins, but lacks the RNR motif (R677 N678 R679 in Ncd). Its similarity to the kinesin-1 neck linker, together with the presence of an adjacent calmodulin-binding helix that regulates KCBP binding to microtubules, likely explain the high affinity docking of the KCBP neck mimic to the motor core. Because the KCBP motor that was analyzed lacked a stalk, movements of the stalk were not observed.

Kar3, a *Saccharomyces cerevisiae* kinesin-14 that functions as a heterodimer with nonmotor partner proteins Vik1 or Cik1, also lacks the RNR motif[55]. Neck mimic docking in Kar3 is inferred to be less stable, consistent with the weaker neck mimic sequence conservation compared to Ncd and KCBP, making heterodimerization with Vik1 or Cik1 and interhead coordination important for Kar3 motility.

The findings we report here – the NcdY485K stalk fluctuations during AMP-PNP binding and neck mimic docking in the MT-bound and detached post-PS states – have not been reported previously. These findings are relevant to previous observations for the role of the neck mimic in kinesin-14 motor proteins. Notably, we observed significant stalk fluctuations during AMP-PNP binding, which were captured by MD simulations and shown to be markedly suppressed upon neck mimic docking. These results extend previous models by showing that the neck mimic not only contributes to force generation but also plays a critical role in stabilizing the stalk conformation during the power stroke. Importantly, our findings imply that the neck mimic produces a plus-end directed swing, which is then converted into a minus-end directed power stroke by the stalk – this highlights a directional coupling mechanism resembling the plus-end directed kinesins.

In plus-end directed kinesin motors, the cover-neck bundle, a two-stranded β-sheet formed by cover strand β0 and neck linker strand β9, is thought to trigger neck linker docking, stabilized by interactions of a conserved neck linker residue (strand β10 N334 in kinesin-1) with strand β7 of the central β-sheet, producing the power stroke[13,56]. Analogously, we observe that kinesin-14 neck mimic residues K671–K676 adopt a conformation similar to strand β9 in the ADP·Pi state of kinesin-1 and our MD simulations suggest that this promotes docking of the full neck mimic onto the motor core. Moreover, arginine residues in the neck mimic region corresponding to strand β10 are present in the kinesin-14 KIFC1, KIFC2, and KIFC motors, which could stabilize the interface between the neck mimic and the motor core. However, the absence of the cover strand and cover-neck bundle in kinesin-14 likely affects the docking of the neck mimic and its stability in head H2 of the NcdY485K crystal structure. Following ATP hydrolysis and microtubule detachment, conformational changes in switch I/II,

including a helix-to-loop transition at the N-terminus of helix α4 and strand-to-loop transitions in the central β-sheet, are observed. These structural changes probably weaken neck mimic interactions with the central β-sheet, destabilizing its docking in the NcdY485K ADP + free Pi state, which causes the stalk to rotate slightly towards the microtubule minus end, but maintain its post-PS orientation.

Kinesin structural changes during Pi release – central β-sheet unfolding & refolding

The formation of loops by β-strands and the high B-factors of the neck mimic, switch I/II and other structural elements at the motor-MT binding interface in the NcdY485K ADP + free Pi state (Fig. 5c) indicate that these regions exhibit high entropy, which is likely to be associated with destabilization of the bound Pi and its release following motor detachment from the microtubule. The strand β4-loop L7-strand β5 cluster is close to the MT-binding surface in the MT-NcdY485K ADP·Pi bound head, and Y485K at the distal end of strand β4/loop L7 touches switch I (Supplementary Fig. 12). Switch I, in turn, senses and interacts with the nucleotide phosphate bound to the active site[57]. The end of strand β6, together with the distal end of strand β4 and loop L10, interact with each other and with the coiled-coil stalk in the pre-PS state (Supplementary Fig. 9d). These strands and loops are coupled to one another by the central β-sheet – the β-strands twist and shorten, acting like a spring to store free energy to drive the working strokes of the motor. The strands and loops form a pathway for transmitting changes at the motor microtubule-binding surface to the nucleotide-binding cleft[40], triggering the power stroke – the free energy is then directed to loop L10 via the active site to drive the recovery stroke. The structural changes at the microtubule-binding interface, active site, neck mimic and stalk during the kinesin-14 cycle act through the central β-sheet, leading to the power stroke upon motor binding to ATP, producing force and microtubule sliding, and then induce Pi release and the motor recovery stroke after ATP hydrolysis and detachment from the microtubule. The central β-sheet thus provides both the coupling and springlike motions that are essential to the energy transduction mechanism. This mechanism is likely to apply to other kinesins, given the high conservation of the structural elements involved across the kinesin superfamily proteins, although it leaves open the possibility of other mechanisms that enhance free energy changes in other kinesin motors[58].

Methods

Protein expression and purification

A plasmid for bacterial expression of NcdY485K (MGSM-H293-K700-His6) was constructed in pMW172[29] using usual recombinant DNA methods. The NcdY485K protein contains 54 residues of the α-helical coiled-coil Ncd stalk joined to the conserved motor domain, but is deleted for the N-terminal tail and ~96 residues of the predicted stalk. The motor domain contains a single residue change of Y485K.

pMW172/NcdY485K was transformed into *E. coli* BL21(DE3) host cells (Novagen), cultured overnight, and grown in 1 L LB media in 2 L flasks (total 8 L) at 37 °C in the presence of 100 µg/ml ampicillin to OD_{600} ~ 0.6, then cooled down in cold water. Expression was induced by adding 0.1 mM isopropyl-α-D-thiogalactopyranoside (IPTG) overnight at 18 °C. Cells were harvested and stored at -80 °C until use. Cells were resuspended in buffer A [50 mM HEPES pH 7.5, 80 mM NaCl, 1 mM $MgCl_2$, 1 mM EGTA, 1 mM DTT, 0.7 µM leupeptin, 2 µM pepstatin A, 1 mM phenylmethylsulfonyl fluoride (PMSF), and 2 mM benzamidine], lysed by sonication and cleared by centrifugation. The lysate was applied to a HiTrap SP ion exchange column (GE Healthcare), washed with 100 mM NaCl in HEM buffer (10 mM HEPES pH 7.5, 1 mM $MgCl_2$, 1 mM EGTA, and 1 mM DTT), and eluted with a linear gradient of 500 mM NaCl in HEM buffer. The second peak of the eluate was concentrated and applied to a Superdex 200 Increase (GE Healthcare) size exclusion chromatography column equilibrated with 100 mM NaCl in HEM buffer for the final step in purification. Protein in the peak fractions was concentrated to ~ 13–14 mg/ml, flash frozen in liquid nitrogen, and stored at -80 °C.

NcdY485K protein for crystallization was expressed essentially as described above, but in *E. coli* Rosetta2 (DE3) pLysS host cells (Novagen). Cells were lysed by sonication in binding buffer (BB; 12 mM Na_2HPO_4/NaH_2PO_4 pH 7.4, 300 mM NaCl, 20 mM imidazole, and 0.5 mM $MgCl_2$). After clearing by centrifugation, the lysate was loaded onto a Ni column for purification by Ni-affinity chromatography. Elution was with BB + 280 mM imidazole, followed by Superdex 200 size exclusion FPLC in HEM200 buffer (HEM + 200 mM NaCl). Purified NcdY485K protein was concentrated, frozen, and stored at − 80 °C.

Tubulin was purified from porcine brains purchased from a meat factory in Kobe, Japan, as described previously[59].

Cryo-EM grid Preparation

Tubulin (60 µM) was incubated in PEMGTP buffer (100 mM PIPES pH 6.8, 1 mM $MgCl_2$, 1 mM EGTA, and 1 mM GTP) at 37 °C for 30 min and microtubules were stabilized by adding 60 µM taxol. NcdY485K-microtubule complexes in different nucleotide states were prepared using essentially the same procedure except for the presence or absence of the nucleotide analogue in the NcdY485K protein solution. For nucleotide-free NcdY485K grid preparation, the purified protein was used. For AMP-PNP, 2 mM AMP-PNP was added to the purified NcdY485K protein and incubated for 10 min. For ADP-AlF_3, 2 mM ADP, 2 mM AlF_3, and 8 mM NaF were incubated with purified NcdY485K for 30 min. Microtubules (4 µl drop of 40 µM dilution) were placed onto a glow-discharged holey carbon grid (R2/1; Quantifoil) prepared on a JEC-3000FC (JEOL). After 30 s, the solution was wicked away with a piece of Whatman No. 1 filter paper and 80 µM of NcdY485K protein in different nucleotide states was applied (4 µl drop), incubated for 1 min, blotted, and plunge-frozen in liquid ethane using a Vitrobot Mark IV (Thermo Fisher Scientific).

Cryo-EM data collection and processing

Cryo-EM data were collected on a JEOL CRYO ARM 300 cryo-electron microscope at SPring-8 in Japan with a cold-field emission gun as the electron source, an in-column Ω filter, using a K3 direct electron detector (Gatan)

in the electron counting mode. Images were collected at a nominal magnification of ×60,000, corresponding to a calibrated pixel size of 0.753 Å. Each movie was recorded in correlated-double sampling (CDS) mode for 2.5 s and subdivided into 50 frames with 50 $e^-/Å^2$ at the specimen. The image shift method automatically acquired the data using SerialEM software[60] with a defocus range of – 0.8 to -1.5 µm. Approximately 6,000–8,000 movies were acquired for each condition, and the total number of images is described in Supplementary Table 2.

Collected movie frames were subjected to Relion implemented motion correction, and the contrast transfer function (CTF) of the movie frames was estimated by CTF in RELION 3.1[61]. To obtain high resolution maps of microtubules decorated by Ncd in different nucleotide states, we employed MiRPv2[32], a method specialized for high resolution single particle analysis and for analyzing the pseudo-helical nature of microtubules with a seam, which can precisely determine the positions of α- and β-tubulins and the seam. First, microtubules on the micrographs were manually picked using the helical mode of RELION (v3.1.4). The selected microtubules were then extracted as particles with a box size of 600 $Å^2$ and box separation distance of 82 Å with 4 x binning. The extracted particles were 3D classified (PF-sorting) into 6 classes of 11- to 16-protofilaments (PF) using low pass filtered 11- to 16-PF microtubules as references. After PF-sorting, we reassigned incorrectly assigned particles in the same filament to the correct protofilament number, assuming that the protofilament number is the same throughout a single microtubule. Because most of the particles were classified as 13- and 14-PF (see Supplementary Fig. 1), we analyzed the predominant 13 and 14 PF classes. In the next step, we aligned the seam position. To improve the signal-to-noise ratio of the particles, neighboring particles in an MT were averaged over 7 segments along the helical axis and were used for 3D classification[62]. The rotation angles were modified to ensure being linear in a microtubule followed the 3D classification. Moreover, X/Y shifts, which center the microtubule particles onto the reference, were also applied to ensure the linearity in a microtubule. To check the seam position, we 3D-classified the refined particles to the possible seam references (i.e., 26 references for a 13-protofilament microtubule, with 13 seam positions and their counterparts translated 1 monomer along the helical axis), and the seam position of particles was corrected according to the classified result. Finally, we reconstructed the particles by re-extracting particles from the micrographs without binning. The corrected particles were C1-reconstructed, and the refined particles were used in the symmetrized reconstruction to improve the resolution. The refined particles were further post-processed to acquire a high-resolution map according to the postprocess procedure of Relion. Figures and movies of cryo-EM structures were made in Chimera or ChimeraX[63,64].

Molecular dynamics simulations

We first built MT-NcdY485K NF and ADP-AlF_3 all-atom models based on the cryo-EM structures, containing three protofilaments, each consisting of three α,β-tubulin dimers (Supplementary Fig. 8a), the neck mimic was not resolved in the NF cryo-EM density map and was excluded from the model. We therefore modeled the neck mimic in the NF structure using Modeller[65]. Coarse-grained (CG) models were built using the "GENESIS-CG-TOOL"[43] from the molecular dynamics (MD) software GENESIS[66]. This tool replaced the C_α atom of each residue with a CG bead, converting the MT-NcdY485K NF and ADP-AlF_3 all-atom models into CG representations (Supplementary Fig. 8a).

We defined two angles, θ and ϕ, to estimate the swing of the stalk, representing the kinesin-14 NcdY485K power stroke (Fig. 4c). The coordinates were set by calculating the center of mass (COM) of three tubulin dimers near NcdY485K (PDB file, chains C, G, L), denoted p1, p2, and p3, respectively. The Z-axis was defined as the normal vector to the microtubule, computed as the product of vectors $\overrightarrow{p_{21}}$ and $\overrightarrow{p_{23}}$, where $\overrightarrow{p_{ij}} = \overrightarrow{p_j} - \overrightarrow{p_i}$, and the X-axis, as the product between the Z-axis vector and $\overrightarrow{p_{21}}$, ensuring orthogonality to Z. Finally, the Y-axis is $\overrightarrow{p_{21}}$. The movement of the stalk was followed by calculating the center of mass (COM) of residues comprising the stalk hinge (V342 to R346 in MT-bound NcdY485K) and the stalk tip (L296 to V300 in both MT-bound and MT-unbound NcdY485K) and defining a vector from the base to the tip of the stalk. The angle between this vector and the Z-axis was defined as θ and the angle between its projection onto the XY-plane and the X-axis was defined as φ.

Equilibrium MD simulations

Equilibrium MD simulations of the NF and ADP-AlF_3 states were performed using the AICG2 + residue-level CG force field[67] and GENESIS v2.1.3[66] compiled with double precision. Simulations were performed with a time step of 1.0×10^1 fs for 1.0×10^7 steps and with fixed number of particles (N), volume (V) and temperature (T) at 300° K. Langevin dynamics was used as the integrator with a friction coefficient γ of 0.01 ps^{-1}. Trajectory data were saved every 100 steps and 100 independent simulations were performed to assess statistical replicability. The same procedure was applied to an NF model in which the neck mimic and NcdY485K 16 aa C-terminus (K671 to K700) were removed. The simulations were performed on a CPU-only platform without GPUs, equipped with an Intel(R) Xeon(R) Gold 6142 processor (2.60 GHz) and 96 GB of RAM.

Some simulations exhibited excessive stalk rotation that would be implausible in cells. Therefore simulations in which the minimum value of φ dropped below zero at any point were excluded from the analysis. In the simulations of the NF state, no implausible data were observed in the presence or absence of the neck mimic and all 100 simulations were included in the analysis for both. By contrast, for the ADP-AlF_3 state, 99 of the 100 simulations were retained in the presence of the neck mimic, while 68 of the 100 simulations were retained in its absence, and these datasets were used for subsequent analysis using Python 3.9.5[68], MDAnalysis 2.7.0[69,70], and Pandas 2.2.3[71]. Figures were plotted using Matplotlib 3.9.4[72] and seaborn 0.13.2[73], and ChimeraX version 1.5 was used to display CG models[64].

Convergence of the simulations was assessed by calculating the RMSD at each time point relative to the starting structure, which was also used as the force field. First, the COM of each simulated structure was determined, then the structure was superimposed with the starting structure using the Kabsch algorithm[74].

RMSD values were calculated for C_α atoms in the aligned structures using MDAnalysis[69,70] (Supplementary Fig. 8d).

Evaluation of neck mimic docking in *Switching Gō* simulations

Switching Gō simulations[44] were performed to simulate conformational changes from the NF pre-PS state to the ADP-AlF_3 post-PS state by applying the ADP-AlF_3 force field to the NF coordinates. The parameters were identical to those used in the equilibrium MD simulations. The simulation protocol consisted of three stages (Supplementary Table 4). First, an equilibrium simulation was performed for 2.0×10^5 steps using the NF force field on the NF structure (stage 1). Next, an energy minimization was carried out for 3.0×10^3 steps by applying the ADP-AlF_3 force field to the structure obtained in stage 1 to suppress large structural forces due to abrupt force field switching. Energy minimization was performed using the steepest descent (SD) algorithm without applying any convergence threshold. Coordinates were output every 10 steps during minimization to monitor structural relaxation (stage 2). Finally, a run of 2.0×10^6 steps was performed with the ADP-AlF_3 force field applied to the minimized structure, during which the conformational transition was induced (stage 3).

As in the equilibrium MD simulations, some trajectories in these simulations exhibited structural changes in stage 3 that involved implausible changes in the stalk angle, which are unlikely to occur under physiological conditions. These trajectories were excluded from the structural analysis. As a result, 79 of the 100 simulations were retained in the presence of the neck mimic and 73 of 100 in its absence. These datasets were used for subsequent analysis. RMSD was calculated at each time point using the starting NF structure as the reference structure, as in the equilibrium simulations (Supplementary Fig. 8d).

Evaluation of neck mimic docking in *Switching Gō* simulations.

When two residues *i* and *j* form a contact in the ADP-AlF_3 state, the equilibrium distance between the two residues is defined as d_{ij}^{eq} and, at any time t, the distance between i and j is $d_{ij}(t)$. A contact between residues i and j is defined as maintained if the following occurs:

$$\left|d_{ij}(t) - d_{ij}^{eq}\right| < 10\ \mathring{A}$$

We assessed neck mimic docking during the conformational transition from NF pre-PS to ADP- AlF_3 post-PS by quantitating the fraction of contacts for the neck mimic (residues K671 to V685) at each time point during the simulation using the contact pairs observed in the ADP-AlF_3 cryo-EM structure. This metric is termed the "neck mimic contact ratio". The time at which the neck mimic contact ratio exceeds 0.95 is defined as the time of neck mimic docking to the motor domain.

We determined the order of docking for residues of the neck mimic and motor domain from the number of maintained contacts between the neck mimic and motor domain residues divided by the maximum number of contacts that the residue forms throughout the simulation. This metric, termed "normalized contact count", was determined at each time point during the structural transition. We assessed the sequential order in which neck mimic residues engage with the motor domain by plotting the normalized contact count for each neck mimic residue in each MD step (Supplementary Fig. 8c). For reference, the residues involved in contacts between the neck mimic and motor domain in the NF and ADP–AlF_3 states are shown in Supplementary Table 4.

Crystallization

Purified protein was thawed, incubated on ice with 5.3 mM Mg^{2+}-ATP for 60 min, then centrifuged for 6 min at 16,630x g and 4 °C. Crystals were grown in hanging drops by mixing 1.3 µl protein + Mg^{2+}-ATP with 1.5 µl reservoir solution, which consisted of 1 ml of 50 mM Na_2HPO_4/KH_2PO_4 pH 6.8, 7 mM DTT, 10 mM $MgCl_2$, 0.8 M NaCl, 13% w/v PEG8000 and 5% glycerol. Crystallization trays were incubated at 16 °C. Crystals appeared in 2 days and were grown at 16 °C for ~6 days before harvesting. Crystals were incubated in cryoprotection buffer (reservoir solution + 25% glycerol), flash frozen, and stored in liquid nitrogen.

X-ray diffraction data collection and processing

A complete diffraction data set was collected at the Advanced Photon Source Synchrotron on NECAT Beamline 24-ID-E with an Eiger detector (Argonne National Laboratory, Chicago, IL USA). The data set was processed using HKL2000[75]. The NcdY485K structure was solved by molecular replacement using the Phaser program[76] from the Phenix crystallographic suite. A wild-type Ncd structure (PDB 1CZ7) was used as the initial search model. PDB 1CZ7 contains two Ncd dimers in the asymmetric unit. Dimer 2, in which a longer α-helical coiled-coil stalk is visible[33], was used to solve the NcdY485K structure. Model building was performed using the Coot program[77] and refinement was carried out using Phenix Refine and REFMAC5[78,79]. Refinement was continued until the R-values converged to 0.25 (R_{free}=0.29) with 3.15 Å resolution. The model has good stereochemistry with all residues within the allowed regions of the Ramachandran plot, as analyzed by MolProbity[80] (Supplementary Table 5). Figures were made in Chimera or ChimeraX[63,64].

Fluorescence assays

NcdY485K intrinsic fluorescence due to tryptophan (Trp) residues was assayed to detect conformational changes that affect the Trp residue environment in different motor states. Assays were performed using FPLC-purified NcdY485K protein[29] at 0.36 to 2.71 µM in 20HEM300 buffer (20 mM HEPES pH 7.2, 1 mM EGTA, 1 mM $MgCl_2$, 300 mM NaCl) and 22 °C in a Cary Eclipse spectrofluorometer. Fluorescence was read before and after a mixing control (with no additions) and after adding 100 mM Na_2HPO_4/KH_2PO_4 pH 6.8. Free Trp at 0.72 to 13.22 µM was assayed as a control, together with controls performed by addition of the same volume

of 20HEM300 buffer instead of Na_2HPO_4/KH_2PO_4. Fluorescence recorded during the assays was corrected for decreases in NcdY485K or free Trp concentration due to the increased volume upon addition of Na_2HPO_4/KH_2PO_4 or buffer, and for photobleaching, using a free Trp photobleaching decay curve (Supplementary Fig. 10). The rate of photobleaching was found to be 0.000517/s for the 20 nm slit width used under the conditions of the assays shown in Fig. 7c, which were performed for 10 s and 274 nm excitation with 358 nm emission for free Trp or 330 nm emission for NcdY485K; PMT voltages (V) were the same as matched control assays in which 20HEM300 buffer was added to the cuvette instead of 100 mM Na_2HPO_4/KH_2PO_4 pH 6.8. Fluorescence spectra (Fig. 7b and Supplementary Fig. 10a) were read using slit widths of either 10–20 nm, and were not corrected for photobleaching, as there was very little change in fluorescence intensity in repeat assays. The NcdY485K + Pi fluorescence decrease shown in Fig. 7c is interpreted to be caused by changes in the central β-sheet of head H2 that expose W473 to solvent. The free Trp + Pi fluorescence decrease is assumed to be due to Trp interactions with Pi. The small NcdY485K + buffer fluorescence decrease was greater in protein that had been freeze-thawed several times before assaying and is attributed to protein unfolding and loss upon mixing (e.g., by binding to the micropipette tip). Assays under different PMT voltage conditions or with a different purification of NcdY485K protein also showed a large decrease in fluorescence with added Pi (deposited in Zenodo as files with names that include the following terms: NcdYK, prep 2). Protocols for the intrinsic fluorescence assays have been deposited in Zenodo with the data files.

β-sheet structural analysis

A crystal structure of NcdY485K (this report), together with crystal structures of four other wild-type or variant or mutant Ncd dimeric motor proteins with a rotated stalk was displayed in Chimera[63] and β-strand length was analyzed (Supplementary Table 6). The crystal structures show chain A (head H1) in a pre-PS state and chain B (head H2) in a post-PS state. A wild-type Ncd crystal structure with both heads in a pre-PS state was analyzed as a control (PDB 1CZ7 dimer 2, chains C and D). The Ncd dimeric motor post-PS heads show shorter strands β7, β6, and β4, which correspond to β-strands 5–7, respectively, in nucleotide-free myosin – these strands in myosin undergo the largest changes between nucleotide states. The shorter head H2 β-strands are due to strand-to-loop transitions – the strands differ in length in different Ncd variants or mutants, potentially reflecting different transition states of head H2 in the crystal structures (shortest β-strands, bold font in Supplementary Table 6). The two heads of previous Ncd dimeric motor crystal structures have been reported to be bound to ADP. By contrast, NcdY485K head H1 is bound to ADP and head H2 to ADP + free Pi.

Analysis of central β-sheet residue movements between the NcdY485K crystal structure heads H1 (ADP) and H2 (ADP + free Pi) was performed by first identifying the residues that comprise each strand of the β-sheet. Residues were included in the analysis if they were present in a β-strand in at least one head of the motor and if the residue and atom numbers matched between the two heads. This allowed us to include the effects of β-strand to loop transitions, which are expected to increase the flexibility of the central β-sheet, and loop conversions to β-strands, which would decrease the β-sheet flexibility. As a result, strands were compared with loops if head H1 and H2 differed in β-sheet structure. The pre-stroke wild-type Ncd structure (1CZ7 dimer 2, chain C and D) was included as a control, but β-sheet residues were defined for the 1CZ7 heads separately from NcdY485K H1 and H2, although using the same criteria. This was necessary because the 1CZ7 structure represents a pre-power stroke state, differing from the post-stroke NcdY485K structure.

Differences in β-strand residue positions and orientations between the two heads of NcdY485K and those of Ncd 1CZ7 dimer 2 were calculated using the Chimera RMSD tool[81]. The Chimera script used to analyze the residue differences is included in the Supplementary Materials. The RMSD output value for each NcdY485K β-strand residue is shown in a heat map (Fig. 6e). The totals shown below the heat map were obtained by squaring the RMSD values, multiplying by the number of atoms in each residue of the β-strand, and summing the products. The β-sheet differences between the NcdY485K and Ncd 1CZ7 structures were compared by calculating the mean β-strand RMSD±SD from the Chimera RMSD output and determining the significance in GraphPad Prism using an unpaired t test (see Fig. 6 legend).

The MT-NcdY485K NF (nucleotide-free) and MT-NcdY485K ADP·Pi (ADP-AlF_3) cryo-EM structures (this report) were also analyzed for β-strand residue differences compared to the MT-unbound state that could be interpreted as central β-sheet twisting or distortional movements (Supplementary Table 3). The MT-NcdY485K NF and MT-NcdY485K ADP·Pi cryo-EM models are somewhat lower resolution (3.24 or 3.99 Å, respectively) than the NcdY485K crystal structure (3.15 Å), and the positions of side groups of the β-strand residues are expected to be less accurate in these structures. We therefore performed C_α-C_α RMSD analysis to provide an estimate of the changes in the β-sheet between the unbound Ncd ADP state and the MT-Ncd nucleotide states. This was done by aligning the NcdY485K crystal structure head H1 β-strand residue C_α atoms with the C_α atoms of the same residues of the MT-bound or unbound head of the cryo-EM models using Matchmaker in ChimeraX v1.6[64]. The RMSD values were displayed by Matchmaker after selecting the NcdY485K β-strands in the Sequence Viewer window and selecting *Also restrict to selection* for NcdY485K head H1 and *Iterate by pruning long atom pairs* in the Matchmaker window prior to running the analysis. Differences were observed for all the pairwise comparisons. The largest RMSD mean value was observed for the comparison of the NcdY485K crystal structure head H1 and H2 (Supplementary Table 3).

This method for estimating β-sheet RMSD values differs from that used for the NcdY485K crystal structure head H1 vs. head H2 and shown in the heat map in Fig. 6e. First, it does not include residues that are present in β-strands in the protein chain under comparison, but not in NcdY485K head H1. Second, Matchmaker uses only the single C_α atom per residue for fitting, rather than other atoms or all atoms of the residue. Third, Matchmaker uses only the paired C_α-C_α atoms to obtain an RMSD value. By contrast, the RMSD analysis shown in Fig. 6e is an all-atom comparison of residues that are present in a β-strand in at least one head of the motor. The methods used to estimate β-sheet RMSD differences shown in Supplementary Table 3 are thus not the same as those

used to produce the heat map in Fig. 6e, since they use only a single point per residue, which is the C_α atom. Exclusion of side chain atoms is expected to result in under-estimates of the actual β-sheet differences. For example, the comparison of NcdY485K head H1 vs. head H2 shown in Supplementary Table 3 gave a β-sheet C_α-C_α RMSD mean difference of 1.154±0.753 Å (mean±SD, $n = 82$ C_α-C_α pairs), compared to an all-atom RMSD mean difference of 1.250±0.230 Å ($n = 11$ strands) for the analysis shown in Fig. 6e (see legend). Because of the methods that were used for the analysis, the RMSD data in Supplementary Table 3 are not directly comparable to the data for the NcdY485K crystal structure shown in Fig. 6e. However, the cryo-EM MT-bound head β-sheet distortional changes are apparent from the C_α-C_α RMSD mean values, and they are also observed in the superpositions of the MT-bound heads with NcdY485K ADP head H1 (Fig. 6b, c) and movies showing morphs between each other, including stick models of the β-strand carbon backbones (Supplementary Movie 1), or between the MT-bound heads and H1 or H2 (Supplementary Movies 2, 4 and 5).

Statistical analysis

Statistical tests were performed in GraphPad Prism or KaleidaGraph (Synergy). Unpaired t tests were used to compare data for two independent groups and one-way analysis of variance (ANOVA) followed by Tukey's Honestly Significant Difference (HSD) pairwise tests was used to compare data sets consisting of more than two independent groups. P values are given in the text or in the legends for the figures in which the data are shown. The ANOVA and Tukey's tests for the NcdY485K β-strand residue C_α-C_α RMSD values that were obtained using the Chimera X Matchmaker tool are shown in Supplementary Table 3.

Data availability

MT-NcdY485K cryo-EM density maps and atomic models have been deposited into the Electron Microscopy Data Bank (EMDB) and the Protein Data Bank (PDB) under the following accession codes: NF 13PF EMD-39,664/PDB ID 8YY2, NF 14PF EMD-39,665/PDB ID 8YY3, AMPPNP 13PF EMD-39,668, AMPPNP 14PF EMD-39,669, ADP-AlF_3 13PF EMD-39,666/PDB ID 8YY4 and ADP-AlF_3 14PF EMD-39,667/PDB ID 8YY5. The cryo-EM raw micrographs will be deposited to EMPIAR. The NcdY485K atomic model coordinates and .mtz file containing the unprocessed x-ray data have been deposited into the PDB under accession code PDB ID 8YUE. The RMSD data shown in Fig. 6e and the fluorimeter data shown in Fig. 7b, c and Supplementary Fig. 10 have been deposited in Zenodo[82] (zenodo.org/records/16929593). A preprint reporting these findings has been deposited in bioRxiv[83] (doi https://doi.org/10.1101/2024.07.29.605428).

Received: 2 September 2025; Accepted: 11 November 2025
Published online: 05 January 2026

References

1. Howard, J. *Mechanics of Motor Proteins and the Cytoskeleton* (Sinauer Associates, Inc., 2001).
2. Kull, F. J. & Endow, S. A. Force generation by kinesin and myosin cytoskeletal motor proteins. *J. Cell. Sci.* **126**, 9–19 (2013).
3. Sweeney, H. L. & Houdusse, A. Structural and functional insights into the myosin motor mechanism. *Annu. Rev. Biophys.* **39**, 539–557 (2010).
4. Bagshaw, C. R. *Biomolecular Kinetics: A step-by-step Guide* (Taylor & Francis/CRC, 2017).
5. Kull, F. J., Sablin, E. P., Lau, R., Fletterick, R. J. & Vale, R. D. Crystal structure of the kinesin motor domain reveals a structural similarity to myosin. *Nature* **380**, 550–555 (1996).
6. Boyer, P. D., Cross, R. L. & Momsen, W. A new concept for energy coupling in oxidative phosphorylation based on a molecular explanation of the oxygen exchange reactions. *Proc. Natl Acad. Sci. USA* **70**, 2837–2839 (1973).
7. Houdusse, A., Szent-Györgyi, A. G. & Cohen, C. Three conformational States of scallop myosin S1. *Proc. Natl. Acad. Sci. USA*. **97**, 11238–11243 (2000).
8. Howard, J., Hudspeth, A. J. & Vale, R. D. Movement of microtubules by single kinesin molecules. *Nature* **342**, 154–158 (1989).
9. Block, S. M., Goldstein, L. S. B. & Schnapp, B. J. Bead movement by single kinesin molecules studied with optical tweezers. *Nature* **348**, 348–352 (1990).
10. Hackney, D. D. Highly processive microtubule-stimulated ATP hydrolysis by dimeric kinesin head domains. *Nature* **377**, 448–450 (1995).
11. Kozielski, F. et al. The crystal structure of dimeric kinesin and implications for microtubule-dependent motility. *Cell* **91**, 985–994 (1997).
12. Rice, S. et al. A structural change in the kinesin motor protein that drives motility. *Nature* **402**, 778–784 (1999).
13. Hwang, W., Lang, M. J. & Karplus, M. Force generation in kinesin hinges on cover-neck bundle formation. *Structure* **16**, 62–71 (2008).
14. Yun, M. et al. Rotation of the stalk/neck and one head in a new crystal structure of the kinesin motor protein, Ncd. *EMBO J.* **22**, 5382–5389 (2003).
15. Heuston, E., Bronner, C. E., Kull, F. J. & Endow, S. A. A kinesin motor in a force-producing conformation. *BMC Struct. Biol.* **10**, 19 (2010).
16. Liu, H. L., Pemble, I. V., Endow, S. A. & C. W. & Neck-motor interactions trigger rotation of the kinesin stalk. *Sci. Rep.* **2**, 236 (2012).
17. Park, H. W. et al. Structural basis of small molecule ATPase Inhibition of a human mitotic kinesin motor protein. *Sci. Rep.* **7**, 15121 (2017).
18. Rayment, I. et al. Three-dimensional structure of myosin subfragment-1: a molecular motor. *Science* **261**, 50–58 (1993).
19. Rayment, I. et al. Structure of the actin-myosin complex and its implications for muscle contraction. *Science* **261**, 58–65 (1993).
20. Endow, S. A. & Higuchi, H. A mutant of the motor protein Kinesin that moves in both directions on microtubules. *Nature* **406**, 913–916 (2000).
21. Endres, N. F., Yoshioka, C., Milligan, R. A. & Vale, R. D. A lever-arm rotation drives motility of the minus-end-directed kinesin Ncd. *Nature* **439**, 875–878 (2006).
22. Yamagishi, M. et al. Structural basis of backwards motion in kinesin-1-kinesin-14 chimera: implication for kinesin-14 motility. *Structure* **24**, 1322–1334 (2016).
23. Endow, S. A. & Waligora, K. W. Determinants of kinesin motor polarity. *Science* **281**, 1200–1202 (1998).
24. Vinogradova, M. V., Reddy, V. S., Reddy, A. S., Sablin, E. P. & Fletterick, R. J. Crystal structure of kinesin regulated by Ca^{2+}-calmodulin. *J. Biol. Chem.* **279** (504–523), 509 (2004).

25. Uyeda, T. Q. P., Abramson, P. D. & Spudich, J. A. The neck region of the myosin motor domain acts as a lever arm to generate movement. *Proc. Natl. Acad. Sci. USA*. **93**, 4459–4464 (1996).
26. Coureux, P. D. et al. A structural state of the myosin V motor without bound nucleotide. *Nature* **425**, 419–423 (2003).
27. Reubold, T. F., Eschenburg, S., Becker, A., Kull, F. J. & Manstein, D. J. A structural model for actin-induced nucleotide release in myosin. *Nat. Struct. Biol.* **10**, 826–830 (2003).
28. Hirose, K., Akimaru, E., Akiba, T., Endow, S. A. & Amos, L. A. Large conformational changes in a kinesin motor catalysed by interaction with microtubules. *Mol. Cell.* **23**, 913–923 (2006).
29. Liu, H. L., Hallen, M. A. & Endow, S. A. Altered nucleotide-microtubule coupling and increased mechanical output by a kinesin mutant. *PLos One*. **7**, e47148 (2012).
30. Chandra, R., Salmon, E. D., Erickson, H. P., Lockhart, A. & Endow, S. A. Structural and functional domains of the *Drosophila* Ncd microtubule motor protein. *J. Biol. Chem.* **268**, 9005–9013 (1993).
31. Stewart, R. J., Thaler, J. P. & Goldstein, L. S. B. Direction of microtubule movement is an intrinsic property of the motor domains of kinesin heavy chain and *Drosophila* ncd protein. *Proc. Natl Acad. Sci. USA* **90**, 5209–5213 (1993).
32. Cook, A. D., Manka, S. W., Wang, S., Moores, C. A. & Atherton, J. A microtubule RELION-based pipeline for cryo-EM image processing. *J. Struct. Biol.* **209**, 107402 (2020).
33. Kozielski, F., De Bonis, S., Burmeister, W. P., Cohen-Addad, C. & Wade, R. H. The crystal structure of the minus-end-directed microtubule motor protein Ncd reveals variable dimer conformations. *Structure* **7**, 1407–1416 (1999).
34. Sindelar, C. V. & Downing, K. H. An atomic-level mechanism for activation of the knesin molecular motors. *Proc. Natl Acad. Sci. USA* **107**, 4111–4116 (2010).
35. Gigant, B. et al. Structure of a Kinesin-tubulin complex and implications for kinesin motility. *Nat. St Mol. Biol.* **20**, 1001–1007 (2013).
36. Sippel, K. H. & Quiocho, F. A. Ion-dipole interactions and their functions in proteins. *Protein Sci.* **24**, 1040–1046 (2015).
37. Song, H. & Endow, S. A. Decoupling of nucleotide- and microtubule-binding in a kinesin mutant. *Nature* **396**, 587–590 (1998).
38. Jumper, J. et al. Highly accurate protein structure prediction with AlphaFold. *Nature* **596**, 583–589 (2021).
39. Lacabanne, D. et al. ATP analogues for structural investigations: case studies of a DnaB helicase and an ABC transporter. *Molecules* **25,** 5268 (2020).
40. Nitta, R., Okada, Y. & Hirokawa, N. Structural model for strain-dependent microtubule activation of Mg-ADP release from Kinesin. *Nat. St Mol. Biol.* **15**, 1067–1075 (2008).
41. Sindelar, C. V. et al. Two conformations in the human kinesin power stroke defined by X-ray crystallography and EPR spectroscopy. *Nat. Struct. Biol.* **9**, 844–848 (2002).
42. Wendt, T. G. et al. Microscopic evidence for a minus-end-directed power stroke in the kinesin motor Ncd. *EMBO J.* **21**, 5969–5978 (2002).
43. Tan, C. et al. Implementation of residue-level coarse-grained models in GENESIS for large-scale molecular dynamics simulations. *PLoS Comput. Biol.* **18**, e1009578 (2022).
44. Yang, S. & Song, C. *Switching Gō-Martini* for investigating protein conformational transitions and associated protein-lipid interactions. *J. Chem. Theory Comput.* **20**, 2618–2629 (2024).
45. Kikkawa, M. & Hirokawa, N. High-resolution cryo-EM maps show the nucleotide binding pocket of KIF1A in open and closed conformations. *EMBO J.* **25**, 4187–4194 (2006).
46. Nitta, R., Kikkawa, M., Okada, Y. & Hirokawa, N. KIF1A alternately uses two loops to bind microtubules. *Science* **305**, 678–683 (2004).
47. Pechatnikova, E. & Taylor, E. W. Kinetic mechanism of monomeric non-claret disjunctional protein (Ncd) ATPase. *J. Biol. Chem.* **272**, 30735–30740 (1997).
48. Möller, M. & Denicola, A. Protein tryptophan accessibility studied by fluorescence quenching. *Biochem. Mol. Biol. Educ.* **30**, 175–178 (2002).
49. Pechatnikova, E. & Taylor, E. W. Kinetics processivity and the direction of motion of Ncd. *Biophys. J.* **77**, 1003–1016 (1999).
50. Foster, K. A., Correia, J. J. & Gilbert, S. P. Equilibrium binding studies of non-claret disjunctional protein (Ncd) reveal cooperative interactions between the motor domains. *J. Biol. Chem.* **273**, 35307–35318 (1998).
51. Chang, Q., Nitta, R., Inoue, S. & Hirokawa, N. Structural basis for the ATP-induced isomerization of kinesin. *J. Mol. Biol.* **425**, 1869–1880 (2013).
52. Chai, P. et al. Cryo-EM reveals the mechanochemical cycle of reactive full-length human dynein-1. *bioRxiv* Preprint https://doi.org/10.1101/2024.05.01.592044 (2024).
53. Ozbudak, E. M., Thattai, M., Lim, H. N., Shraiman, B. I. & Van Oudenaarden A. Multistability in the lactose utilization network of Escherichia coli. *Nature* **427**, 737–740 (2004).
54. Popchock, A. R. et al. The mitotic kinesin-14 KlpA contains a context-dependent directionality switch. *Nat. Commun.* **8**, 13999 (2017).
55. Rank, K. C. et al. Kar3Vik1, a member of the kinesin-14 superfamily, shows a novel kinesin microtubule binding pattern. *J. Cell. Biol.* **197**, 957–970 (2012).
56. Khalil, A. S. et al. Kinesin's cover-neck bundle folds forward to generate force. *Proc. Natl. Acad. Sci. USA*. **105**, 19247–19252 (2008).
57. Sablin, E. P., Kull, F. J., Cooke, R., Vale, R. D. & Fletterick, R. J. Crystal structure of the motor domain of the kinesin-related motor Ncd. *Nature* **380**, 555–559 (1996).
58. Hwang, W., Lang, M. J. & Karplus, M. Kinesin motility is driven by subdomain dynamics. *Elife* **6**, e28948 (2017).
59. Castoldi, M. & Popov, A. V. Purification of brain tubulin through two cycles of polymerization-depolymerization in a high-molarity buffer. *Protein Expr Purif.* **32**, 83–88 (2003).
60. Mastronarde, D. N. Automated electron microscope tomography using robust prediction of specimen movements. *J. Struct. Biol.* **152**, 36–51 (2005).
61. Zivanov, J. et al. New tools for automated high-resolution cryo-EM structure determination in RELION-3. *Elife* **7**, e42166 (2018).
62. Zhang, R. & Nogales, E. A new protocol to accurately determine microtubule lattice seam location. *J. Struct. Biol.* **192**, 245–254 (2015).
63. Pettersen, E. F. et al. UCSF Chimera–a visualization system for exploratory research and analysis. *J. Comput. Chem.* **25**, 1605–1612 (2004).
64. Pettersen, E. F. et al. UCSF ChimeraX: structure visualization for researchers, educators, and developers. *Protein Sci.* **30**, 70–82 (2021).
65. Sali, A. & Blundell, T. L. Comparative protein modelling by satisfaction of spatial restraints. *J. Mol. Biol.* **234**, 779–815 (1993).
66. Jung, J. et al. GENESIS 2.1: High-performance molecular dynamics software for enhanced sampling and free-energy calculations for atomistic, coarse-grained, and quantum mechanics/molecular mechanics models. *J. Phys. Chem. B*. **128**, 6028–6048 (2024).
67. Li, W., Wang, W. & Takada, S. Energy landscape views for interplays among folding, binding, and allostery of calmodulin domains. *Proc. Natl. Acad. Sci. USA*. **111**, 10550–10555 (2014).
68. Python Software Foundation v. 3.9.5 python.org/. (2021).
69. Michaud-Agrawal, N., Denning, E. J., Woolf, T. B. & Beckstein, O. MDAnalysis: a toolkit for the analysis of molecular dynamics simulations. *J. Comput. Chem.* **32**, 2319–2327 (2011).
70. Gowers, R. J. et al. in *Proceedings of the 15th Python in Science Conference.* (eds S. Benthall & S. Rostrup) 98–105 (2016).
71. Pandas v. 2.3.3. zenodo.org, (2024).

72. Hunter, J. D. & Matplotlib A 2D graphics environment. *CiSE* **9**, 90–95 (2007).
73. Waskom, M. L. Seaborn: statistical data visualization. *JOSS* **6**, 3021 (2021).
74. Kabsch, W. A solution for the best rotation to relate two sets of vectors. *Acta Cryst. A*. **32**, 922–923 (1976).
75. Otwinowski, Z. & Minor, W. Processing of X-ray diffraction data collected in oscillation mode. *Methods Enzymol.* **276**, 307–326 (1997).
76. McCoy, A. J. et al. Phaser crystallographic software. *J. Appl. Crystallogr.* **40**, 658–674 (2007).
77. Emsley, P., Lohkamp, B., Scott, W. G. & Cowtan, K. Features and development of Coot. *Acta Crystallogr. D Biol. Crystallogr.* **66**, 486–501 (2010).
78. Liebschner, D. et al. Macromolecular structure determination using X-rays, neutrons and electrons: recent developments in phenix. *Acta Crystallogr. D Struct. Biol.* **75**, 861–877 (2019).
79. Vagin, A. A. et al. REFMAC5 dictionary: organization of prior chemical knowledge and guidelines for its use. *Acta Crystallogr. D Biol. Crystallogr.* **60**, 2184–2195 (2004).
80. Williams, C. J. et al. MolProbity: more and better reference data for improved all-atom structure validation. *Protein Sci.* **27**, 293–315 (2018).
81. Meng, E. C., Pettersen, E. F., Couch, G. S., Huang, C. C. & Ferrin, T. E. Tools for integrated sequence-structure analysis with UCSF chimera. *BMC Bioinform.* **7**, 339 (2006).
82. Wang, M. Y., Imasaki, T., Nitta, R. & Endow, S. A. RMSD and Trp assays for structural analysis of a motor with increased mechanical output reveals new transitions in kinesin microtubule motility. *Zenodo* **v5** https://doi.org/10.5281/zenodo.16929593 (2025).
83. Shibata, S. et al. Structural transitions in kinesin minus-end directed microtubule motility. *bioRxiv* Preprint https://doi.org/10.1101/2024.07.29.605428 (2024).

Acknowledgements

We thank G. Christoph, C. Gopalasingam, and K. Kato for cryo-EM data collection management and support at SPring-8 and K. Chin for research management support. S.A.E. thanks S. Zhang and J.J. Gooley for Duke-NUS NBD Programme laboratory space, D.M. Virshup for Duke-NUS CSCB Programme hospitality, T.G. Oas for guidance on the fluorescence assays, E.C. Meng for information about Chimera Matchmaker, and Z. Meng for help with data analysis. This work was supported by grants from the Japan Society for the Promotion of Science KAKENHI (22K06809 to TI, 22H02795 and 21H05254 to RN); AMED-CREST from the Japan Agency for Medical Research and Development (AMED; JP21gm1610003 to TI and JP21gm0810013 to RN); Japan Science and Technology Agency [JST/FOREST (JPMJFR214K to TI); JST/Moonshot (JPMJMS2024 to RN)]; Takeda Science Foundation and Mochida Memorial Foundation for Medical and Pharmaceutical Research to TI and RN; and the Uehara Memorial Foundation, Bristol-Myers Squibb, and Hyogo Science and Technology Association to RN. The cryo-EM experiments were performed at SPring-8 with the approval of the Japan Synchrotron Radiation Research Institute (JASRI) (Proposal No. 2021B2536, 2022A2536, 2022B2542, 2023A2542, 2023B2537, 2024B2531, 2024B2532) and AMED-BINDS JP25ama121001. NcdY485K purification and crystallization were supported by Duke-NUS Medical School funds to SAE and NcdY485K structural analysis by NIH NICHD 1R21HD105034-01A1 Grant Award to SAE. JS acknowledges Ministry of Education National University of Singapore AcRF Tier-1 (R154-000-A72-114) and Tier-2 (R-154-000-B03-112) funding support. Diffraction data were collected at the Northeastern Collaborative Access Team beamlines, funded by NIH NIGMS P30 GM124165, using resources of the APS, a US DOE Office of Science User Facility operated for the DOE Office of Science by Argonne National Laboratory under Contract No. DE-AC02-06CH11357, using APS beamline 24-ID-E. The Eiger 16 M detector on the 24-ID-E beam line is funded by NIH-ORIP HEI Grant S10OD021527.

Author contributions

Conceptualization: SAE, TI, RN; Investigation: TI, HS, RN, SAE, SS, YW, CJ, DULT; Data analysis: SS, TI, MYW, CJ, RN, SAE, HH, DULT, YS, JS; Data curation: TI, SS, CJ, SAE, MYW; Funding acquisition: TI, RN, SAE, JS; Project administration: TI, SAE, RN, YS, JS; Supervision: TI, SAE, RN, YS, JS; Writing original draft: SAE, TI, RN; Figures and Tables: TI, SS, MYW, SAE, RN; Review/editing: TI, SAE, MYW, RN, SS, JS, CJ, YS, YW; Final review: All authors.

Declarations

Competing interests

The authors declare no competing interests.

Additional information

Supplementary Information The online version contains supplementary material available at https://doi.org/10.1038/s41598-025-28573-7.

Correspondence and requests for materials should be addressed to T.I., S.A.E. or R.N.